The Asgard archaeal ESCRT-III system forms helical filaments and remodels eukaryotic membranes, shedding light on the emergence of eukaryogenesis

Nataly Melnikov[1,2], Benedikt Junglas[3$], Gal Halbi[4$], Dikla Nachmias[1,2], Erez Zerbib[1,2], Alexander Upcher[5], Ran Zalk[5], Carsten Sachse[3,6*], Ann Bernheim-Groswasser[4,5], Natalie Elia[1,2*]

1 Department of Life Sciences, Ben-Gurion University of the Negev, Beer Sheva 84105, Israel

2 National Institute for Biotechnology in the Negev (NIBN), Ben-Gurion University of the Negev, Beer Sheva 84105, Israel

3 Ernst-Ruska Centre for Microscopy and Spectroscopy with Electrons, ER-C-3/Structural Biology, Forschungszentrum Jülich, 52425 Jülich, Germany

4 Department of Chemical Engineering, Ben-Gurion University of the Negev, Beer Sheva 84105, Israel

5 Ilse Katz Institute for Nanoscale Science and Technology, Ben Gurion University of the Negev, Beer Sheva 84105, Israel

6 Department of Biology, Heinrich Heine University, Universitätsstr. 1, 40225 Düsseldorf, Germany

$ these authors contributed equally to this work.

* Corresponding authors:

Structural analysis:

Carsten Sachse

Phone: +49 2461/61-2030

Email: c.sachse@fz-juelich.de

All other subjects:

Natalie Elia

Phone: 972-8-6428735

Email: elianat@post.bgu.ac.il

ABSTRACT

The ESCRT machinery mediates membrane remodeling in numerous processes in cells including cell division and nuclear membrane reformation. The identification of ESCRT homologs in Asgard archaea, currently considered the closest ancestor of eukaryotes, implies a role for ESCRTs in the membrane remodeling processes that occurred during eukaryogenesis. Yet, the function of these distant ESCRT homologs is mostly unresolved. Here we show that Asgard ESCRT-III proteins of the Lokiarcheota self-assemble into helical filaments, a hallmark of the ESCRT system. We determined the cryo-EM structure of the filaments at 3.6 Å resolution and found that they share features of bacterial and eukaryotic ESCRT-III assemblies. Markedly, Asgard ESCRT-III filaments bound and deformed eukaryotic-like membrane vesicles. Oligonucleotides facilitated the assembly of ESCRT-III filaments and tuned the extent of membrane remodeling. The ability of Asgard archaeal ESCRTs to remodel eukaryotic-like membranes, which are fundamentally different from archaeal membranes, and the structural properties of these proteins places them at the junction between prokaryotes and eukaryotes, substantiating a role for ESCRTs in eukaryogenesis.

50 GRAPHICAL ABSTRACT

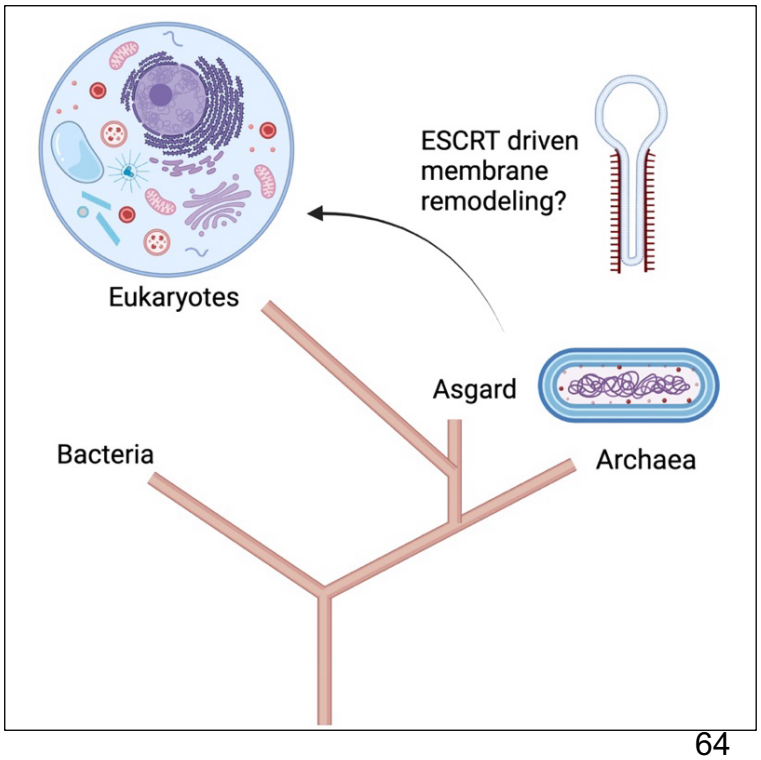

64

65 INTRODUCTION

66

67 The Asgard superphyla, manifest a unique branch that, according to current
68 evolutionary theories, is considered to be the closest prokaryotic relative of eukaryotes.
69 All Asgard archaeal species were found to encode for Eukaryotic Signature Proteins
70 (ESPs), that carry cellular functions that until recently were considered as exclusive to
71 eukaryotes (*1-3*). Thus, Asgard proteins potentially hold the core functions of ancient
72 eukaryotic cellular machines. Of particular interest, are ESPs with membrane
73 remodelling capabilities, as these proteins may contribute to the establishment of
74 cellular compartmentalization during eukaryogenesis. Indeed, Asgard archaea encode
75 for several eukaryotic membrane remodelling machineries including the SNARE
76 complex, BAR domains proteins and the ESCRT machinery (*1, 3, 4*). Among these
77 machineries, ESCRTs are the most conserved and are encoded by all Asgard species
78 discovered up to date, suggesting that they carry essential functions in these unique
79 prokaryotes (*5, 6*).

80

81 The ESCRT machinery constitute one of the most robust and versatile cellular
82 apparatus for membrane constriction and fission. Proteins of the machinery are
83 encoded by all domains of life and were shown to mediate membrane remodelling in a
84 wide range of eukaryotic cellular membranes including plasma membrane, nuclear
85 membrane and endocytic membranes (*7, 8*). Moreover, ESCRT-mediated processes
86 span a large spectrum of length scales, from less than 100 nm for vesicle release to up
87 to 1 μm for cell division. How the ESCRT complex mediate membrane remodelling in
88 this large landscape of membrane sources and length scales is mostly unknown (*9*).
89
90 The eukaryotic ESCRT system is composed of five subfamilies, i.e. ESCRT 0-III and the
91 AAA-ATPase VPS4. Within this complex, ESCRT-III (named CHMPs in animal cells)
92 and VPS4 manifest the minimal unit required for driving membrane fission (*9, 10*).
93 According to current models, membrane constriction and scission are mediated by
94 polymerization of ESCRT-III proteins into helical hetero-filaments and their remodelling
95 by VPS4, seen in vitro and in cells (*10-19*). However, the large number of proteins
96 within the ESCRT-III subfamily —twelve in humans and eight in yeast - have challenged
97 mechanistic studies of the basic function of the machine.
98
99 Reduced, simplified ESCRT-III systems have been identified in prokaryotes including in
100 bacteria and archaea (named Vipp1 and PspA in bacteria and CdvB in archaea) (*7, 20,*
101 *21*). While the bacterial homologs were shown to remodel membranes, no VPS4 was
102 identified in this system so far. ESCRTs encoded by TACK archaea were shown to
103 participate in cell division, suggesting functional similarities between the eukaryotic and
104 archaeal ESCRT systems (*22-25*). Within the archaeal domain the Asgard ESCRT
105 system is considerably closer to the eukaryotic system. While all other archaea encode
106 only for ESCRT-III and VPS4 homologs, Asgard archaea encode for homologs of the
107 complete ESCRT system (ESCRT-I-III and VPS4) (*6, 7*). Additionally, the sequence of
108 Asgard ESCRT-III/VPS4 proteins is more closely related to those of eukaryotes than to
109 other archaeal ESCRT systems (named CDV) (*5, 20*). Lastly, VPS4 homologs of
110 Asgard archaea were shown to functionally interact with eukaryotic ESCRTs in both
111 yeast and mammalian cells (*5, 26*). Notably, the Asgard ESCRT-III subfamily is

112 substantially reduced compared to eukaryotes with only two ESCRT-III proteins (named
113 here CHMP1-3 and CHMP4-7) encoded in some species including Loki and Heimdall
114 archaeota (*1, 5, 7, 26*). Hence, the Asgard ESCRT system may constitute a more basic
115 version of the ESCRT machinery, which holds the core capabilities of eukaryotic
116 ESCRTs, and could have been involved in membrane remodelling processes that
117 occurred during eukaryogenesis. Yet, the function, organization, and properties of
118 Asgard ESCRT-III complexes as well as their ability to remodel membranes are mostly
119 unknown.
120
121 In this work, we provide the first evidence that Asgard ESCRT-III complexes share
122 functional similarities with eukaryotic ESCRTs. Using purified ESCRT-III homologs
123 encoded by the most abundant Asgard phyla, Lokiarchaeota (Loki), we show that the
124 Asgard ESCRT-III protein CHMP4-7 can self-assemble, on its own and in the presence
125 of CHMP1-3, into helical tubes that resemble those of eukaryotes (*15, 18, 19, 27*). The
126 frequency of helical tubes was increased in the presence of short ssDNA oligos, while
127 no filaments could be observed upon DNAse treatment. Moreover, we determined the
128 cryo-EM structure of helical CHMP 4-7 tubes in the presence of CHMP 1-3 and DNA at
129 a resolution of 3.6 Å. The 36 nm wide tubular assemblies are built from protomers
130 adopting the canonical ESCRT-III fold while they share characteristic intersubunit
131 contacts with bacterial and eukaryotic ESCRT-III polymers. Finally, we found that Loki
132 ESCRT filaments, formed under any of these conditions, are able to bind and deform
133 small unilamellar vesicles (SUVs) comprised of eukaryotic-like synthetic phospholipids.
134 Hence, Loki ESCRT-III assemble into helical filaments that are affected by
135 oligonucleotides and are capable of remodelling eukaryotic-like membranes.
136
137 RESULTS
138
139 Current phylogenic models suggests that eukaryotes integrate from the archaeal Asgard
140 clade (Fig. 1A). ESCRT-III proteins encoded in eukaryotes polymerize into helical
141 filaments - a hallmark of ESCRT-III organization that is thought to be essential for their
142 function in membrane remodeling (*8, 28*). Polymerization is mediated by the snf7

143 domain that is conserved in both archaea and eukaryotes, but the polymerization
144 properties of their ancestor Asgard ESCRT-III homologs has not been examined (*5, 20,*
145 *26*). To investigate the assembly properties of Asgard ESCRT-III proteins, we purified
146 recombinant versions of the ESCRT-III proteins CHMP4-7 and CHMP1-3, encoded by
147 the Loki GC14_75 strain (KKK44605.1 and KKK42122.1, respectively). Purified proteins
148 were then subjected to polymerization reaction (see methods) and visualized by
149 negative-stain TEM and cryo-EM. Recombinant full-length CHMP4-7 spontaneously
150 self-assembled into helical filaments (Fig. 1B), while no evidence for polymerization
151 could be detected for purified CHMP1-3 using a range of experimental conditions (Fig.
152 S1). The overall shape of CHMP4-7 filaments, seen by negative-stain EM, resembled
153 those previously described for eukaryotic or bacterial ESCRT-III filaments (*15, 18, 19,*
154 *29*). CHMP4-7 polymers were predominantly seen as long, thin and curved filaments or
155 as rod-shaped tubes (Fig. 1B, see arrows and Fig. 1C). A Moiré pattern of parallel,
156 periodic stripes was detected in the CHMP4-7 tube structures by cryo-EM, supporting a
157 helical tube organization (Fig. 1C, D). The outer diameter of the CHMP4-7 tubes was
158 variable, ranging between 35 to 55 nm (averaged diameter 44 ± 30.9 nm). Tube length
159 was typically between 300 - 450 nm (Fig. 1E). The diameter of Loki CHMP4-7 helical
160 tubes was slightly larger than the diameters measured for human CHMP1B (~25nm) or
161 the bacterial ESCRT-III homologs PspA (~21 nm), but was in the range of diameters
162 measured for human CHMP2A-CHMP3 (38 - 43 nm) (*18, 19, 29*). Collectively, these
163 data indicate that Loki CHMP 4-7 spontaneously self-assemble into the typical helical
164 tube organization described for the ESCRT-III complex.
165
166 Next, we examined the effect of CHMP1-3, which did not polymerize on its own, on the
167 ESCRT-III filaments. To this end, full lengths Loki CHMP4-7 and CHMP1-3 were co-
168 incubated at different ratios and subjected to polymerization reaction. While no
169 polymers were seen at 1:1 CHMP4-7-CHMP1-3 ratio, helical tubes could be readily
170 observed at 2:1, 4:1 and 6:1 ratios (Fig. 2 and S2A). Notably, helical tubes assembled in
171 the presence of both CHMP4-7 and CHMP1-3 were morphologically distinct from helical
172 tubes assembled using only CHMP4-7. First, their outer diameter was significantly
173 smaller and less diverse (28 ± 1.6 nm vs 44 ± 30.9 nm for CHMP4-7/CHMP1-3 4:1 ratio

174 and CHMP4-7 alone, respectively) (Fig. 2B, left panel). Second, helical tubes formed in
175 the presence of both CHMP4-7 and CHMP1-3 were significantly longer than those
176 formed by the CHMP4-7 homo-polymer (>X1.5 folds increase for 2:1 and 4:1 ratios)
177 (Fig. 2B, right panel). Third, the morphology of the CHMP4-7/CHMP1-3 helical tube was
178 slightly different: tubes appeared to be more curved and periodic stripes, were readily
179 detected in negative stain images, suggesting that packing of the helical tube is less
180 tight in the presence of CHMP1-3 (Fig. 2A). Additionally, unpacked filaments,
181 resembling a telephone cord were observed, further supporting a continuous helical
182 tube assembly (Fig. S2B). The phenotypic changes observed in the presence of
183 CHMP1-3 were not induced upon substituting CHMP1-3 with purified GFP or by
184 increasing the concentration of CHMP4-7, suggesting that they are specifically
185 contributed by CHMP1-3 (Fig. S2C). Therefore, the Loki ESCRT-III protein CHMP4-7
186 self-assemble into helical filaments, with CHMP1-3 affecting the properties of these
187 filaments. These findings are in line with previous observations obtained for human
188 ESCRT-III CHMP1B helical filaments, which also formed a narrower, more uniform
189 tubes in the presence of IST1(*30*). The realization that both human and Asgard ESCRT-
190 III proteins assemble into helical filaments that can adopt a narrower, more uniform tube
191 shape in the presence an additional subunit, suggests that this is a conserved property
192 of the ESCRT-III system.
193
194 Recent work from our laboratory showed that purified Loki CHMP4-7 binds short DNA
195 oligonucleotides (*26*). Human CHMP1B, exhibited similar properties and a recently
196 solved cryo-EM structure of human CHMP1B/IST1 filaments demonstrated direct
197 interactions between the ESCRT-III filament and nucleic acids (*26, 31*). We, therefore,
198 set to examine the effect of short DNA oligonucleotides on the self-assembly properties
199 of Asgard ESCRT-III filaments. A five-fold increase in the occurrence of helical tubes
200 was observed for CHMP4-7/CHMP1-3 helical tubes that were assembled in the
201 presence of ssDNA, in negative stain TEM images (Fig. 3A-C and Fig. S3A). Addition of
202 dsDNA, comprising the same sequence, did not induce this effect (Fig. S3B). Incubating
203 CHMP1-3 with ssDNA, did not induce polymerization, further supporting the inability of
204 CHMP1-3 to self-assemble in the absence of CHMP4-7 (Fig. S3C). The presence of

205 DNA affected the properties of CHMP4-7/CHMP1-3 helical tubes. Helical tubes formed
206 in the presence of ssDNA were wider and slightly longer (averaged diameters: 40±4 nm
207 vs. 29.4±4.6 nm; averaged lengths: 777.5 ±210 nm vs. 535 ±119 nm for helical tubes
208 polymerized with and without ssDNA, respectively) (Fig. 3D). Moreover, filaments were
209 less curved, and the periodic stripes observed in negative stain images could not be
210 observed (Fig. 3A). Addition of ssDNA also increased the frequency of helical tubes
211 formed by CHMP4-7 alone, but to a lesser extent (three folds), without affecting their
212 characteristic length or diameter (Fig. 3B-D and Fig. S3D). Helical tube formation was
213 completely abolished for both CHMP 4-7/CHMP1-3 and CHMP4-7 filaments in the
214 presence of DNase, resulting aggregates formation, further supporting a role for DNA in
215 ESCRT-III helical tube assembly (Fig. 3E and Fig. S3E).
216
217 Given the higher frequency of ESCRT-III helical filaments obtained for CHMP4-
218 7/CHMP1-3 filaments in the presence of ssDNA, we set out to resolve the cryo-EM
219 structure of the filaments. In our cryo-EM micrographs, we found two types of filaments:
220 straight tube/rod-like polymers with variable diameters and thinner highly curved
221 polymers (as described above) (Fig. 4A, Fig. S4A). Firstly, the curved filaments had
222 diameters of 6 to 15 nm and showed distinct features in their 2D class averages such as
223 saw-tooth-like spikes emanating sideways from the filament including, in some cases, a
224 central smooth line (Fig. S4B). Nevertheless, we were unable to generate reliable 3D
225 reconstructions, likely due to their variable curvature and remaining heterogeneity.
226 Secondly, the rod-shaped filaments had diameters ranging from 30 to over 45 nm. The
227 2D class averages showed well-defined spikes at the filament rims and a Christmas-
228 tree like pattern (Fig. 4B), overall closely resembling PspA rods (*29*). We were able to
229 determine the structure of 36 nm PspA-like rods at a global resolution of 3.6 Å and a
230 local resolution ranging from 3.0 Å at the inner rod wall to 6.0 Å at the outer tube wall
231 (Fig. 4C-E). The rods are arranged by helical symmetry with 1.05 Å rise and 173.9 º
232 rotation. In the lumen of the rods, weak cylindrical density was found close to the inner
233 wall of the rods at approx. 13 nm radial position (Fig. S4C). We relied on the strong
234 density to build a model for Loki CHMP4-7 α1-5 into the density (Fig. 5A-B), while no
235 density was found for helices α0 and α6. Despite the presence of CHMP1-3 and ssDNA

236 in the sample and the described effects on frequency and morphology of the
237 assemblies, we could not identify any corresponding density in the cryo-EM map.
238 CHMP1-3 is, therefore, not a regular member of the symmetric rod assemblies while it
239 may be part of the curved filaments, involved in nucleation or occasionally bound to the
240 rod assemblies. The structured elements of CHMP 4-7 adopt the canonical ESCRT-III
241 fold: α1-3 form an extended hairpin, connected to α4 via a short linker (E117-P120 Fig.
242 5B inset). Helix α4 is separated in two parts by a short loop at G146 and connected to
243 α5 by an extended linker (I154-E159). The monomers are arranged in a j+4 repeat,
244 where α5 of chain j packs perpendicularly against the tip of the hairpin of j+4 (Fig. 5C),
245 forming the typical ESCRT-III assembly motif known from IST1B/CHMP1B (*18*). In the
246 assembly, helices α1-4 make up the wall of the rods, while α5 together with the tip of
247 the α1+2 hairpin forms the spikes on the outside of the wall (Fig. S4D and 5D).
248 Consequently, although unresolved, α6 is likely located outside the rods while α0 points
249 into the lumen perhaps as part of the weak density found inside the rods. The
250 electrostatic surface of the rod assembly reveals a distinct polarity with one negatively
251 and one positively charged end (Fig. S4E). The same interfaces likely also stabilize the
252 layers of the rod assembly by electrostatic interactions.
253
254 Loki CHMP4-7 adopts the canonical ESCRT-III fold in the open form and the assembly
255 resembles typical features of ESCRT-III tubes including the conserved motif between
256 α1/2-α5. Comparing the CHMP4-7 rods with ESCRT-III tube-like assemblies of other
257 domains of life, we found that their architecture is most similar to the bacterial
258 assemblies that have a α5-hairpin structure emanating from the tubular wall and giving
259 rise to the characteristic spikes in the projections (Fig. 5E top). In contrast, in eukaryotic
260 assemblies such as IST1 and CHMP1B the α5-hairpin structure does not protrude from
261 the assembly, thereby forming smooth tubes. In CHMP4-7 rods of Asgard, α5 only
262 interacts with a single hairpin at the bottom end, which is a common feature in
263 eukaryotic ESCRT-III assemblies, while in bacteria top and bottom ends of α5 are
264 interacting with two hairpins connecting two layers of the assembly (Fig. 5E bottom).
265 Additionally, on the monomer level, CHMP4-7 more closely resembles the eukaryotic
266 ESCRT-III proteins: firstly, the bacterial ESCRT-IIIs have more extended α0 and α2+3

267 helices (corresponding to aa 10-20, aa 108-123 in the consensus sequence Fig. S4F).
268 Secondly, the linker between α3 and α4 is longer and contains more helix breaking
269 residues in the bacterial ESCRT-IIIs (i.e., G156, G157 and G159 in Vipp1). Therefore,
270 the Loki CHMP4-7 assembly more closely resembles the bacterial configuration with the
271 characteristic spike while the Loki CHMP4-7 monomer adopts a conformation closer to
272 previously determined eukaryotic structures including the α1/2-α5 interaction motif.
273
274 Eukaryotic and bacterial ESCRT-IIIs were shown to bind and deform membranes *in*
275 *vitro* and in cells (*21, 28, 29, 32*). To determine whether ESCRTs encoded by Asgard
276 archaea carry the ability to remodel membranes, we incubated Loki ESCRT-III pre-
277 assembled filaments with small unilamellar vesicles (SUVs, ~100 nm) composed of
278 negatively charged eukaryotic-like phospholipids (1:1, PC:PS). Under these conditions,
279 ESCRT-III filaments, were found to intimately interact with SUVs under any of the
280 conditions tested (including in the presence of ssDNA) (Fig. 6A, B and Fig. S5). We
281 identified four main types of ESCRT-III-SUV interactions: (1) Attachment of the SUV to
282 the outside surface of the tube, which was associated with flattening of the vesicle at the
283 filament-vesicle interface; (2) Docking of the SUV at the tip of the helical tube; (3)
284 Invagination of the SUV to the interior of the ESCRT-III tube; and (4) Dramatic
285 remodeling of both the SUV and the ESCRT-III tube (see examples in Fig. 6C, left
286 panel). Combinations of several types of interactions on the same filament were also
287 observed, indicating that these interactions are not mutually exclusive. In addition, we
288 occasionally observed a docked SUV invaginating into the helical tube (Fig. 6B, left
289 panel, Fig. 6D and sup movies 1, 2), suggesting that these two types of interactions
290 represent successive steps. Invaginations of more than one vesicle to the same tube
291 could be observed, giving rise to the formation of a complex membrane system with
292 several vesicles internalized into one another (Fig 6B). The characteristic periodic
293 stripes of the ESCRT-III filament could often be detected at the exterior of the filament-
294 vesicle complex, suggesting that the observed morphologies result from internalization
295 of vesicles into the ESCRT-III helical tube followed by deformation of the tube. Loki
296 ESCRT III filaments also interacted with neutrally charged SUVs (100% PC) but to a
297 lesser extent, (27% vs. 15% of the total SUVs interacted with ESCRT-III tubes upon

incubation with PC:PS vs PC vesicles, respectively), predominantly exhibiting attachment of the SUV to the exterior of the helical tube (Fig. S6). Therefore, Loki ESCRT-III filaments associate with membrane vesicles and deform negatively charged vesicles via the interior of the tube (see proposed model in Fig. 6E).

Last, we asked whether the composition of ESCRT-III helical tubes, described here, affect their capabilities to remodel membranes. To this end, we quantified the frequencies of the different types of filament-vesicle interactions we defined, at the various assembly conditions. No difference in frequencies were observed for helical filaments that assembled in the presence or absence of CHMP1-3 (CHMP4-7/CHMP1-3 vs CHMP4-7), suggesting that CHMP1-3 does not significantly contribute to membrane interactions. The presence of DNA, however, affected the distributions of ESCRT-III-SUV interactions, as follows (Fig. 6C): First, the association of vesicles with the outside surface of the helical tube (outside, type 1) was considerably enriched (No DNA, <15%; with DNA, >35%). Second, interactions with the tip of the filament (docking, type 2) and invagination of the vesicle (inside, type 3) were significantly enriched. Finally, the most significant difference was the abundance of the complete remodeling events (remodeling, type 4) (no DNA ~80%, with DNA, ~5%;), suggesting that the presence of DNA inhibits this terminal tube-vesicle interaction stage. The effect of DNA on Loki-ESCRT-III induced membrane remodeling appeared to be irreversible, as addition of DNase to pre-established tube-SUV complexes did not lead to extensive membrane remodeling (Fig. S5C). Therefore, Loki ESCRT-III filaments are capable of interacting and remodeling lipid membranes, both in the presence and absence of DNA, but the extent of remodeling appear to be attenuated by the presence of DNA.

DISCUSSION

In this work, we provide the first evidence to show that, Asgard ESCRT-III proteins assemble into helical tubes that resemble those of their eukaryotic homologs and remodel membranes. These findings confirm that ESCRT homologs encoded by Asgard archaea are functionally related to their eukaryotic homologs. We further provide data to

329 support a role for DNA in the assembly of Asgard ESCRT-III filaments. Finally, by using
330 SUVs composed of eukaryotic phospholipids, which are fundamentally different from
331 archaeal lipids, we demonstrate that the Asgard ESCRT-III could, in-principle, contribute
332 to the membrane remodeling processes that occurred during eukaryogenesis and gave
333 rise to the complex phospholipids-based endomembrane system of eukaryotes.
334
335 Our data point to similarities between the human and Asgard ESCRT-III systems.
336 Firstly, the nature of self-assembly appear to be conserved. Similar to the human
337 CHMP1B/IST1 complex, Loki CHMP4-7 was found to polymerize alone or in the
338 presence of CHMP1-3, with the former exhibiting a wider, more variable diameter (*30*).
339 What controls the diameter of the ESCRT-III helical tube is currently unknown. Notably,
340 while IST1 was found to form a layer on the outside of the CHMP1B tube, CHMP1-3
341 could not be detected in our cryo-EM structure suggesting that it obtains a different
342 mode of operation. Regardless of the mechanism, the realization that both human and
343 Asgard ESCRT-III filaments can adopt a wide range of diameters that can be tuned by
344 the addition of another ESCRT-III components, strongly suggest that this is a conserved
345 feature of the ESCRT-III system. Therefore, a basic feature of the ESCRT-III system
346 may be their ability to assemble into adaptable filaments that can be tuned, by
347 additional ESCRT-III proteins, to adopt specific shapes. Such a model can explain how
348 the ESCRT-III system executes the large repertoire of membrane remodeling processes
349 in cells, which greatly vary in scales and topologies (*7, 8*).
350
351 The determined cryo-EM structure of CHMP4-7 helical filaments reveals the canonical
352 ESCRT-III fold made of 6 α-helices including the conserved α1/2-α5 packing equally
353 present in Loki archaea. For eukaryotes and Loki archaea, we detected a number of
354 residue omissions in helices α2+α3 and the linker between α3 and α4, whose
355 associated properties appear to be dispensable in the context of ESCRT evolution and
356 may be responsible for functional diversification of different isoforms. The basic
357 structural arrangement of the molecule in the CHMP4-7 assembly resembles that of
358 previously determined bacterial ESCRT-III proteins PspA and Vipp1 (*29, 32*). In both
359 cases, the hairpin formed by α1/α2 emanates from the assembly giving rise to

360 characteristic spikes in the EM images. Another feature that is closer to the determined
361 eukaryotic assemblies CHMP1B and IST1 is that helix α5 contacts only a single α1/2
362 hairpin as opposed to contacting two α1/2 hairpins described for bacterial ESCRT-III
363 proteins (*18*). This feature makes eukaryotic as well as Loki rods less tightly packed
364 potentially offering additional access for binding partners and thus opening up the
365 possibility to functional modulation and regulation of membrane remodeling by other
366 isoforms of the ESCRT-III family.
367
368 The topology of membrane binding, described here for Loki ESCRT-IIIs, involves
369 invagination of the membrane by the ESCRT-III tube. Although the conventional
370 topology attributed to the ESCRT complex is reversed, as described for the CHMP2A-
371 CHMP3 co-polymer (*19, 27*), membrane binding via the interior of the tube has been
372 reported for the human CHMP1B/IST1 polymer (*30*), and for the bacterial ESCRT-III
373 homologs Vipp1 and PspA (*29, 32*). Consistently, in the cryo-EM structure of Loki
374 ESCRT-III the N terminus, which is associated with membrane binding, is facing the
375 interior of the helical tube. Whether internal membrane binding topology represents the
376 preferred topology of ancient ESCRTs or is a consequence of the, in vitro, experimental
377 system is yet to be determined. Regardless, these similarities suggest that the ESCRT-
378 III membrane remodeling properties reported here are a common property of the
379 ESCRT system in all domains of life.
380
381 Our results highlight DNA as an essential Loki ESCRT-III partner. Self-assembly of the
382 Loki ESCRT-III polymers into high-ordered helical tubes was enhanced in the presence
383 of short ssDNA oligonucleotides, and helical tubes could not be found in the presence of
384 DNase. While the determined cryo-EM structure of Loki ESCRT-III, reported here, does
385 not reveal any density of DNA, a cryo-EM structure of CHMP1B/IST1 filaments shows
386 the presence of DNA in the inner side of the tube and nucleotides were detected in the
387 cryo-EM structure of the bacterial ESCRT-III Vipp1 (*31, 32*). Perhaps the DNA reside in
388 the lumen of the rods seen in the unresolved weak cylindrical density of the Loki
389 ESCRT-III cryo-EM structure.
390

391 Notably, in the ESCRT homologous archaeal CDV system, CDVA, was reported to bind
392 DNA. The exact role of DNA in ESCRT-III filaments assembly is yet to be determined
393 but the accumulating evidence for nucleotide binding in prokaryotic and eukaryotic
394 ESCRTs supports the notion that oligonucleotides binding is another property of the
395 ESCRT-III machine that is conserved in all domains of life.
396
397 The mechanisms by which ssDNA affects the extent of membrane remodeling are
398 unclear. The presence of ssDNA may change the biophysical properties of the tube,
399 thereby resisting the deformation of the tube needed to facilitate membrane remodeling
400 from within. Alternatively, ssDNA and membranes may compete over the same binding
401 sites. Recent results from our laboratory showed that removal of a positively charged N
402 terminal domain, conserved in Asgard CHMP4-7 proteins, from Loki CHMP4-7 abolish
403 DNA binding (*26*). Indeed, the N terminal region of CHMP4-7 is facing the inner side of
404 the tube in the cryo-EM structure (*26*). A plausible scenario, therefore, is that both DNA
405 and membrane binding are mediated via the positively charged N terminal patch located
406 at the interior of the tube. As a result, the presence of ssDNA will reduce the
407 interactions of the tube with the membrane, resulting in a reduced membrane
408 remodeling. Consistent with this model, SUV invaginations were barely detected using
409 neutrally charged SUVs. Future experiments allowing direct visualization of ESCRT-III
410 proteins, DNA, and the membrane at high resolution are needed to examine these
411 models and resolve the intimate relationship between these three partners.
412
413 Overall, the tubular Loki ESCRT-III filaments characterized here, share more similar
414 characteristics to bacterial PspA and Vipp1 and human CHMP1B/IST1 filaments than
415 eukaryotic Vps24 or Snf-7 filaments. Filaments of both Asgard ESCRT-III and human
416 CHMP1B, were shown to assemble into helical polymers that exhibit a constricted, more
417 uniform diameter in the presence of an additional ESCRT-III (CHMP1-3 and IST1,
418 respectively); both filaments were reported to bind DNA in vitro; and both deformed
419 membranes via binding to the inner side of the filamentous tube. Consistently, we
420 recently showed that both Loki CHMP4-7 and human CHMP1B associate with
421 chromatin when expressed in mammalian cells (*26*). We therefore suggest that Asgard

422 ESCRT-IIIs are functionally more similar to CHMP1B in the eukaryotic ESCRT-III
423 system. The findings that the overall structure of the Loki ESCRT-III helical tube
424 resemble that of the bacterial PspA while the intermolecular interactions between the
425 ESCRT-III helixes are more similar to the ones found in CHMP1B, support the notion
426 that the Asgard ESCRT system is an intermediate between the prokaryotic and
427 eukaryotic systems.
428
429 The biological function of Asgard ESCRTs has yet to be defined. The findings that Loki
430 ESCRT-III filaments can bind both DNA and membranes raises a few attractive
431 possibilities. First, given the established role of ESCRTs in cell division in TACK
432 archaea and in eukaryotes, it is possible that the ESCRT machinery manifest a basic
433 cell division machinery capable of orchestrating DNA segregation and membrane
434 splitting (*22-25*). In this regard, the ability of DNA to retain extensive membrane
435 deformation may represent a biological mechanism to avoid premature membrane
436 constriction during cell division. Second, the ESCRT complex may have been involved
437 in nuclear membrane formation during eukaryogenesis, by bringing together
438 membranes and DNA and facilitating DNA encapsulation by membranes. In this
439 respect, mammalian ESCRT-III proteins have been shown to mediate sealing of the
440 nuclear membrane post cell division and to regulate the attachment of heterochromatin
441 to the newly formed nuclear envelope (*33-35*). Moreover, we recently reported that Loki
442 CHMP4-7 is targeted to the nucleus when over expressed in eukaryotic cells (*26*).
443 Finally, the membrane binding experiments performed here were done using
444 eukaryotic-like phospholipids, which are fundamentally different from archaeal lipids but
445 may resemble the lipid composition of the newly formed nuclear membrane. Therefore,
446 the ESCRT-III system encoded by Asgard archaea could have contributed to the
447 membrane remodeling that occurred during the formation of the phospholipids-based
448 nuclear membrane.
449
450
451
452

453 MATERIALS AND METHODS

454 Cloning

455 Open reading frames (ORFs) from Loki MAG sp. GC14_75, encoding for CHMP1-3 and
456 CHMP4-7 genes were obtained from NCBI (accession numbers KKK42122.1,
457 KKK44605.1, respectively) were amplified by PCR and sub-cloned into pSH21 vector
458 subsequently to the TEV cleavage tag that followed an N terminal polyhistidine and
459 MBP protein tags (a kind gift from Eyal Gur, BGU, Israel) (*36*). Plasmids were verified
460 by sequencing.

461

462 Protein Expression and Purification

463 pSH21 plasmids containing Loki CHMP1-3 or CHMP4-7 were expressed Escherichia
464 coli BL21 strain and incubated in LB 50 µg/mL Ampicillin at 37°C until reaching O.D. of
465 0.6. Then, induction with 0.5 mM IPTG was performed and the cultures were grown at
466 30°C for 3-4 hours. Cells were then resuspended and lysed by sonication in buffer A (25
467 mM Hepes pH= 8, 500 mM NaCl, 10% glycerol, 15 mM 2-mercaptoethanol, 10 mM
468 imidazole) supplemented with protease inhibitor cocktail (cOmplete ultra-tablets, EDTA-
469 free, Roche) and 500 µg/ml DNase I (10104159001; Roche Diagnosis GmbH, Manheim,
470 Germany), and the supernatant was clarified by centrifugation (25,000 g, 40 mins, 4°C).
471 For CHMP4-7 purification, supernatant was subjected to HisPur™ Ni-NTA Resin
472 (88222; Thermo Fisher Scientific, Weltham, MA) column and eluted in buffer B (buffer A
473 supplemented with 50 mM imidazole). Protein tags were then removed using a TEV
474 protease (1 mg/10 mg protein) in buffer C (50mM Tris-HCL pH=7.4, 10% glycerol, 500
475 mM NaCl, 15 mM 2-mercaptoethanol). Finally, a second Ni-NTA step was performed
476 using buffer C and the flow-through was collected.
477 For CHMP1-3 purification, supernatant was subjected to Ni-NTA column and eluted in
478 buffer B. Samples were then subjected to amylose resin (E8021; NEB, Frankfurt,
479 Germany) in buffer D (20mM Tris pH=7.4, 500 mM NaCl, 10mM β-Mercaptoethanol,
480 10% Glycerol) and eluted in buffer D supplemented with 10mM maltose. Protein tags
481 were then removed using a TEV protease (1 mg/10 mg protein) in buffer C (50mM Tris-
482 HCL pH=7.4, 10% glycerol, 500 mM NaCl, 15 mM 2-mercaptoethanol). Finally, a

483 second Ni-NTA step was performed using buffer C and the flow-through was collected.
484 Purified proteins were verified my mass spectrometry.
485
486 For polymerization, proteins were incubated in buffer E (25mM Tris pH=7.6, 50 mM KCl)
487 for 5 hours at RT at the indicated conditions. For DNA experiments, buffer E was
488 supplemented with ATCCACCTGTACATCAACTCGCCCGGCGGCTCGATCAGCG (40
489 bases probe, 10 μM), ss or ds at the indicted concentrations. DNase I (10104159001;
490 Roche Diagnosis GmbH, Manheim, Germany) was added at 20 mg/ml concentrations
491 when indicated. Homo polymerization of CHMP1-3 was examined at a range of pH (5.0-
492 8.8), different salt concentrations (0-500 mM NaCl). Polymerization could not be
493 observed under any of these conditions (Fig. S1).
494
495 Preparation of small unilamellar vesicles (SUVs)
496 Chloroform Lipid solutions (DOPC or DOPS) were purchased from Avanti Polar Lipids
497 Inc. (Albaster, AL, USA catalog number 850375, 840035). Lipid mixtures of
498 DOPC/DOPS 1:1 molar ratio and pure DOPC were prepared at a total concentration of
499 1 mg/ml in Tris 20 mM, KCl 50 mM, pH 7.8 were prepared. Each lipid suspension was
500 extruded 20 times via a 100 nm polycarbonate membrane using a mini-extruder (Avanti
501 Polar Lipids, Alabaster, AL, USA). In the final stage, the vesicles were mixed with the
502 Asgard Loki ESCRT-III filaments. All experiments were done with 8 μM ESCRT-III and
503 124 μM vesicles in a buffer of Tris 25 mM, KCl 50 mM, at pH 7.6. DNase was added to
504 the indicated conditions at 20mg/ml concentrations for one hour post vesicle-ESCRT-III
505 incubation.
506
507 Negative stain grid preparation and imaging
508 The negative stain samples for TEM analysis were prepared in the following way: 300
509 mesh copper grids (Ted Pella, Prod No. 01813-F) were glow discharged to enhance
510 hydrophilicity of their surface. Next, 2.5 μL of the sample was applied on to the grid and
511 the excess liquid was blotted with filter paper after 1 minute. The grid was dried in air for
512 1 minute, following by applying 5 μL of uranyl acetate 2% solution (SPI CAS# 6159-44-
513 0) for negative staining to increase the sample contrast. Next, the grid was blotted once

514 more to remove the excess uranyl acetate. Finally, the grid was dried in air before
515 insertion into the microscope. Imaging of the samples was performed with Thermo
516 Fisher Scientific Talos F200C transmission electron microscope operating at 200 kV.
517 The images were taken with Ceta 16M CMOS camera.
518
519 Cryo-electron microscopy
520 **Sample preparation**: 3 µL of proteins / proteins-phospholipids mix samples were gently
521 deposited on glow discharged Quantifoil R 1.2/1.3 holey carbon grids (Quantifoil Micro
522 Tools GmbH, Germany). Samples were manually blotted for four seconds at room
523 temperature and vitrified by rapidly plunging into liquid ethane using a home-built
524 plunging apparatus. The frozen samples were stored in liquid nitrogen until imaging.
525 **Micrograph acquisition.** For an initial data set, samples were loaded under cryogenic
526 conditions and imaged in low dose mode on either a FEI Tecnai F30 Polara microscope
527 (FEI, Eindhoven) operated at 300 kV or a Glacios (Thermo-Fisher Scientific) operated at
528 200 kV. On the Polara, micrographs were loaded under cryogenic conditions and
529 imaged in low dose mode on a FEI Tecnai F30 Polara microscope (FEI, Eindhoven)
530 operated at 300 kV. Micrographs were collected using SerialEM, at a calibrated pixel
531 size of 1.1 Å by a K2 Summit direct electron detector fitted behind an energy filter
532 (Gatan Quantum GIF) set to ±10 eV around zero-loss peak with total electron dose of
533 80 ē/Å2. Each dose-fractionated movie had 50 frames, micrographs sums were aligned
534 in SerialEM. On the Glacios, micrographs were collected using Tomo (Single
535 micrograph) at a calibrated pixel size of 0.87 Å by a Falcon 4i direct electron detector
536 fitted behind a Selectris X energy filter set to ±5 eV around zero-loss peak with total
537 electron dose of 30 e^-/Å2. The final dataset used for was collected on 300 kV Titan
538 Krios G4 (ThermoFisher Scientific) electron microscope equipped with a Biocontinuum
539 K3 (Gatan) detector operated by EPU (ThermoFisher Scientific) (see details Table 1).
540 Dose-fractionated movie frames (30 frames per movie) were acquired at a nominal
541 defocus of 1.5 to 3 µm with a calibrated pixel size of 1.36 Å and a total dose of 30 e^-/$Å^2$.
542 **Helical reconstruction.** For the initial dataset, movie frames were gain-corrected,
543 dose-weighted, and aligned using cryoSPARC Live (*37*). Initial 2D classes were
544 produced using the auto picker implemented in cryoSPARC Live. The following image

545 processing steps were performed using cryoSPARC. The classes with most visible
546 details were used as templates for the filament tracer (50 Å spacing, 50 Å low-pass
547 filter) The resulting filament segments were extracted with 1000 px box size (Fourier
548 cropped to 300 px) and subjected to multiple rounds of 2D classification. The remaining
549 segments were sorted by rod diameter and 2D class averages of the most abundant
550 diameter for initial symmetry guesses in PyHI (*38*). Initial symmetry estimates were
551 validated by helical refinement in cryoSPARC and selection of the helical symmetry
552 parameter yielding a reconstruction with typical ESCRT-III features and the best
553 resolution. For the main dataset, movie frames were gain-corrected, dose-weighted,
554 and aligned using cryoSPARC Live (*37*). Initial 2D classes were produced using the
555 auto picker implemented in cryoSPARC Live. The following image processing steps
556 were performed using cryoSPARC. The classes were separated by filament type (PspA-
557 like rods and curved filaments). Classes with most visible detail were used as templates
558 for the template picker (50 Å spacing). The resulting curved filament segments were
559 extracted with 400 px box size (Fourier cropped to 200 px) and subjected to multiple
560 rounds of 2D classification. The remaining segments were sorted by curvature. Only the
561 least curved segments were kept. No regular helical symmetry could be identified for
562 these filaments, and initial attempts with *ab initio* reconstruction did not yield consistent
563 maps. The PspA-like rods were extracted with 800 px box size (Fourier cropped to 200
564 px) and subjected to multiple rounds of 2D classification. The remaining segments were
565 sorted by diameter. The previously determined helical symmetry was used for an initial
566 reconstruction of the most abundant rods (after re-extraction with 600 px box size,
567 Fourier cropped to 300 px). The corresponding segments were classified by
568 heterogeneous refinement and followed by 3D classifications using the initial helical
569 reconstructions as templates. The resulting helical reconstructions were subjected to
570 multiple rounds of helical refinement including the symmetry search option. For the final
571 polishing, the segments were re-extracted at 600 px without Fourier cropping and
572 subjected to helical refinement including non-uniform refinement. Higher-order
573 aberrations were corrected using global and local CTF-refinement. The local resolution
574 distribution and local filtering for the resulting map was performed using cryoSPARC (as

shown in Fig 4E). The resolution of the final reconstruction was determined by Fourier shell correlation (auto-masked, FSC=0.143).

Cryo-EM map interpretation and model building. The handedness of the maps was determined by rigid-body fitting the hairpin of an Alphafold2 (*39, 40*) prediction of Loki CHMP4-7 into the final map using ChimeraX (*41, 42*) and flipped accordingly. Predictions of Loki CHMP 1-3 and CHMP 4-7 monomers were flexibly MDFF fitted to the 3D reconstruction using ISOLDE (*43*). Only the CHMP4-7 model fitted the secondary structure and large residue pattern present in the map. The CHMP1-3 model was discarded. The CHMP4-7 monomer model was truncated to the parts covered by the map (aa 15-172) and manually refined in ISOLDE. Subsequently, the model was subjected to auto-refinement with *phenix.real_space_refine* (*44*). The auto-refined model was checked/adjusted manually in Coot (*45*). The respective helical symmetry was applied to the model to create assemblies of 60 monomers in ChimeraX and the assembly structure was subjected to another cycle of auto-refinement (with NCS restraints and refinement) using *phenix.real_space_refine* (*44*). After the final inspection, the models were validated in *phenix.validation_cryoem (46) /Molprobity (47).*

Cryo-tomography. Micrographs were acquired using the same setups as of the cryo-EM micrographs. Pixel size at the sample plane on the Polara was 2.3 Å, and 1.9 Å on the Glacios. On the Polara, the camera was operated in counting mode at a dose rate of 6−7 ē/pixels/sec, tilt series of 41 exposures from −21° to +60° and back to -60° in 3° intervals and a total dose of ~ 120 ē /Å^2 were collected with Serial-EM. On the Glacios, the camera was operated in counting mode at a dose rate of 2−3 ē/pixels/sec. Fiducials-free, dose-symmetric tilt series of 61 exposures from −60° to +60° in 2° intervals and a total dose of ~120 ē /Å^2 were collected with Tomo. Tilt series were aligned, and tomograms were reconstructed using eTomo (IMOD4.11 package) (*48*). Movies were generated in imageJ.

Measurements and statistical analysis

Filament length and diameter measurements were performed in Velox software version 3.5 (Thermo Fisher Scientific, Inc.).

Statistical analysis was performed in Graph Pad Prism version 9.00 (La Jolla, CA, USA). Normality was tested using the D'Agostino-Pearson test. For three or more groups, statistical significance was determined by one-way analysis of variance (ANOVA) Kruskal-Wallis test followed by Dunn's post hoc test or by one-way analysis of variance (ANOVA) followed by Tukey post hoc test, for multiple comparisons. Pearson chi-squared test was used to determine the difference in the distribution of the assembled polymers. P values in all figures are as follows: * p- value ≤ 0.1, **p- value ≤ 0.01, ***p- value ≤ 0.001, ****p- value ≤ 0.0001. Bars in all plots indicate mean values and standard deviation of the mean.

ACKNOWLEDMENTS

We thank the laboratories of Eyal Gur (BGU) and Eyal Arbely (BGU) for their practical advice on proteins expression and purifications and for kindly sharing their reagents and equipment with us. We also thank Itzik Mizrahi (BGU) and Ori Avinoam (WIS) for constructive feedback on the project. Last, we thank all members of the Elia lab for critical feedback throughout the project. The Elia laboratory is funded by the Israeli Science Foundation (ISF) Grant no. 1323/18. ABG is grateful to the Israel Science Foundation for financial support (grant 2101/20). The authors gratefully acknowledge the electron microscopy training, imaging, and access time granted by the life science EM facility of the Ernst-Ruska Centre at Forschungszentrum Jülich. The authors gratefully acknowledge the computing time granted by the JARA Vergabegremium and provided on the JARA Partition part of the supercomputer JURECA at Forschungszentrum Jülich (*49*).

AUTHOR CONTRIBUTIONS

NE and DN conceptualized the project. NM performed and analyzed all experiments. GH and AB, were in charge of experiments using SUVs. AU acquired negative stain TEM images. RZ, BJ and CS acquired and analyzed cryo-EM data. BJ and CS built and refined the atomic models. NE, DN, AB and RZ were involved in experimental design

and data analysis. NE, BJ and CS wrote the manuscript. All authors read and revised the manuscript.

Competing Interest Statement: We declare no competing interests.

668 REFERENCES

669 1. K. Zaremba-Niedzwiedzka *et al.*, Asgard archaea illuminate the origin of eukaryotic
670 cellular complexity. *Nature* **541**, 353-358 (2017).
671 2. F. MacLeod, G. S. Kindler, H. L. Wong, R. Chen, B. P. Burns, Asgard archaea: Diversity,
672 function, and evolutionary implications in a range of microbiomes. *AIMS Microbiol* **5**, 48-
673 61 (2019).
674 3. A. Spang *et al.*, Complex archaea that bridge the gap between prokaryotes and
675 eukaryotes. *Nature* **521**, 173-179 (2015).
676 4. E. Neveu, D. Khalifeh, N. Salamin, D. Fasshauer, Prototypic SNARE Proteins Are Encoded
677 in the Genomes of Heimdallarchaeota, Potentially Bridging the Gap between the
678 Prokaryotes and Eukaryotes. *Curr Biol* **30**, 2468-2480 e2465 (2020).
679 5. Z. Lu *et al.*, Coevolution of Eukaryote-like Vps4 and ESCRT-III Subunits in the Asgard
680 Archaea. *mBio* **11**, (2020).
681 6. T. Hatano *et al.*, Asgard archaea shed light on the evolutionary origins of the eukaryotic
682 ubiquitin-ESCRT machinery. *Nat Commun* **13**, 3398 (2022).
683 7. Y. Caspi, C. Dekker, Dividing the Archaeal Way: The Ancient Cdv Cell-Division Machinery.
684 *Front Microbiol* **9**, 174 (2018).
685 8. J. H. Hurley, ESCRTs are everywhere. *EMBO J* **34**, 2398-2407 (2015).
686 9. Y. A. M. Alonso, S. M. Migliano, D. Teis, ESCRT-III and Vps4: a dynamic multipurpose tool
687 for membrane budding and scission. *FEBS J* **283**, 3288-3302 (2016).
688 10. J. McCullough, L. A. Colf, W. I. Sundquist, Membrane fission reactions of the mammalian
689 ESCRT pathway. *Annu Rev Biochem* **82**, 663-692 (2013).
690 11. C. Caillat, S. Maity, N. Miguet, W. H. Roos, W. Weissenhorn, The role of VPS4 in ESCRT-III
691 polymer remodeling. *Biochem Soc Trans* **47**, 441-448 (2019).
692 12. S. Maity *et al.*, VPS4 triggers constriction and cleavage of ESCRT-III helical filaments. *Sci*
693 *Adv* **5**, eaau7198 (2019).
694 13. B. E. Mierzwa *et al.*, Dynamic subunit turnover in ESCRT-III assemblies is regulated by
695 Vps4 to mediate membrane remodelling during cytokinesis. *Nat Cell Biol* **19**, 787-798
696 (2017).
697 14. A. K. Pfitzner *et al.*, An ESCRT-III Polymerization Sequence Drives Membrane
698 Deformation and Fission. *Cell* **182**, 1140-1155 e1118 (2020).
699 15. W. M. Henne, N. J. Buchkovich, Y. Zhao, S. D. Emr, The endosomal sorting complex
700 ESCRT-II mediates the assembly and architecture of ESCRT-III helices. *Cell* **151**, 356-371
701 (2012).
702 16. I. Goliand *et al.*, Resolving ESCRT-III Spirals at the Intercellular Bridge of Dividing Cells
703 Using 3D STORM. *Cell Rep* **24**, 1756-1764 (2018).
704 17. J. Guizetti *et al.*, Cortical constriction during abscission involves helices of ESCRT-III-
705 dependent filaments. *Science* **331**, 1616-1620 (2011).
706 18. J. McCullough *et al.*, Structure and membrane remodeling activity of ESCRT-III helical
707 polymers. *Science* **350**, 1548-1551 (2015).
708 19. S. Lata *et al.*, Helical structures of ESCRT-III are disassembled by VPS4. *Science* **321**,
709 1354-1357 (2008).

710 20. B. P. Frohn, T. Hartel, J. Cox, P. Schwille, Tracing back variations in archaeal ESCRT-based
711 cell division to protein domain architectures. *PLoS One* **17**, e0266395 (2022).
712 21. J. Liu *et al.*, Bacterial Vipp1 and PspA are members of the ancient ESCRT-III membrane-
713 remodeling superfamily. *Cell* **184**, 3660-3673 e3618 (2021).
714 22. A. C. Lindas, E. A. Karlsson, M. T. Lindgren, T. J. Ettema, R. Bernander, A unique cell
715 division machinery in the Archaea. *Proc Natl Acad Sci U S A* **105**, 18942-18946 (2008).
716 23. R. Y. Samson, T. Obita, S. M. Freund, R. L. Williams, S. D. Bell, A role for the ESCRT
717 system in cell division in archaea. *Science* **322**, 1710-1713 (2008).
718 24. R. Y. Samson *et al.*, Molecular and structural basis of ESCRT-III recruitment to
719 membranes during archaeal cell division. *Mol Cell* **41**, 186-196 (2011).
720 25. G. Tarrason Risa *et al.*, The proteasome controls ESCRT-III-mediated cell division in an
721 archaeon. *Science* **369**, (2020).
722 26. D. Nachmias *et al.*, Asgard ESCRT-III and VPS4 reveal conserved chromatin binding
723 properties of the ESCRT machinery. *ISME J*, (2022).
724 27. K. Azad *et al.*, in *bioRxiv*. (2022).
725 28. Y. Olmos, The ESCRT Machinery: Remodeling, Repairing, and Sealing Membranes.
726 *Membranes (Basel)* **12**, (2022).
727 29. B. Junglas *et al.*, PspA adopts an ESCRT-III-like fold and remodels bacterial membranes.
728 *Cell* **184**, 3674-3688 e3618 (2021).
729 30. H. C. Nguyen *et al.*, Membrane constriction and thinning by sequential ESCRT-III
730 polymerization. *Nat Struct Mol Biol* **27**, 392-399 (2020).
731 31. N. Talledge *et al.*, in *bioRxiv*. (2018).
732 32. T. K. Gupta *et al.*, Structural basis for VIPP1 oligomerization and maintenance of
733 thylakoid membrane integrity. *Cell* **184**, 3643-3659 e3623 (2021).
734 33. G. H. Pieper, S. Sprenger, D. Teis, S. Oliferenko, ESCRT-III/Vps4 Controls
735 Heterochromatin-Nuclear Envelope Attachments. *Dev Cell* **53**, 27-41 e26 (2020).
736 34. Y. Olmos, L. Hodgson, J. Mantell, P. Verkade, J. G. Carlton, ESCRT-III controls nuclear
737 envelope reformation. *Nature* **522**, 236-239 (2015).
738 35. M. Vietri *et al.*, Spastin and ESCRT-III coordinate mitotic spindle disassembly and nuclear
739 envelope sealing. *Nature* **522**, 231-235 (2015).
740 36. Y. Elharar *et al.*, Survival of mycobacteria depends on proteasome-mediated amino acid
741 recycling under nutrient limitation. *EMBO J* **33**, 1802-1814 (2014).
742 37. A. Punjani, J. L. Rubinstein, D. J. Fleet, M. A. Brubaker, cryoSPARC: algorithms for rapid
743 unsupervised cryo-EM structure determination. *Nat Methods* **14**, 290-296 (2017).
744 38. X. Zhang, Python-based Helix Indexer: A graphical user interface program for finding
745 symmetry of helical assembly through Fourier-Bessel indexing of electron microscopic
746 data. *Protein Sci* **31**, 107-117 (2022).
747 39. J. Jumper *et al.*, Highly accurate protein structure prediction with AlphaFold. *Nature*
748 **596**, 583-589 (2021).
749 40. M. Mirdita *et al.*, ColabFold: making protein folding accessible to all. *Nat Methods* **19**,
750 679-682 (2022).
751 41. T. D. Goddard *et al.*, UCSF ChimeraX: Meeting modern challenges in visualization and
752 analysis. *Protein Sci* **27**, 14-25 (2018).

42. E. F. Pettersen *et al.*, UCSF ChimeraX: Structure visualization for researchers, educators, and developers. *Protein Sci* **30**, 70-82 (2021).
43. T. I. Croll, ISOLDE: a physically realistic environment for model building into low-resolution electron-density maps. *Acta Crystallogr D Struct Biol* **74**, 519-530 (2018).
44. P. V. Afonine *et al.*, Real-space refinement in PHENIX for cryo-EM and crystallography. *Acta Crystallogr D Struct Biol* **74**, 531-544 (2018).
45. P. Emsley, B. Lohkamp, W. G. Scott, K. Cowtan, Features and development of Coot. *Acta Crystallogr D Biol Crystallogr* **66**, 486-501 (2010).
46. P. V. Afonine *et al.*, New tools for the analysis and validation of cryo-EM maps and atomic models. *Acta Crystallogr D Struct Biol* **74**, 814-840 (2018).
47. C. J. Williams *et al.*, MolProbity: More and better reference data for improved all-atom structure validation. *Protein Sci* **27**, 293-315 (2018).
48. D. N. Mastronarde, Automated electron microscope tomography using robust prediction of specimen movements. *J Struct Biol* **152**, 36-51 (2005).
49. T. P., JURECA: Data Centric and Booster Modules implementing the Modular Supercomputing Architecture at Jülich Supercomputing Centre. *Journal of large-scale reseach facilities JLSRF* **7**, 182-184 (2021).
50. A. M. Waterhouse, J. B. Procter, D. M. Martin, M. Clamp, G. J. Barton, Jalview Version 2--a multiple sequence alignment editor and analysis workbench. *Bioinformatics* **25**, 1189-1191 (2009).
51. P. Di Tommaso *et al.*, T-Coffee: a web server for the multiple sequence alignment of protein and RNA sequences using structural information and homology extension. *Nucleic Acids Res* **39**, W13-17 (2011).

TABLES

Table 1. Data collection, image processing, and model refinement.

Movies	12,751
Magnification	63 kx
Voltage (kV)	300
Total dose (e^-/ Å ^{2})	30
Defocus range (μm)	1.5 to 3
Physical pixel size (Å)	1.36
Detector	Gatan K3
Symmetry imposed	1.05 Å rise 173.9 º rotation C1
Final no. of segments (ASUs)	228,688 (11,205,712)
Global map resolution (Å, FSC = 0.143)	3.55
Local map resolution range (Å, FSC = 0.5)	3.0 -6.0
Initial model used (PDB code)	AF2 prediction
Model refinement	
Model resolution	3.5
CC mask	0.76
CC box	0.29
CC peaks	-0.19
CC volume	0.78
CC ligands	-
Map sharpening B-factor (Å^2)	-76
Model composition	
Nonhydrogen atoms	1251
Protein	1251
RMSDs	
Bond lengths (Å)	0.007
Bond angles (°)	0.909
Validation	
MolProbity score	1.34
Clashscore	3.57
Rotamer outliers (%)	0.74
Ramachandran plot	
Favored (%)	96.79
Allowed (%)	3.21
Disallowed (%)	0.0
Deposition IDs	
EMDB	50583
PDB	9FN1

793 FIGURES AND FIGURES LEGENDS

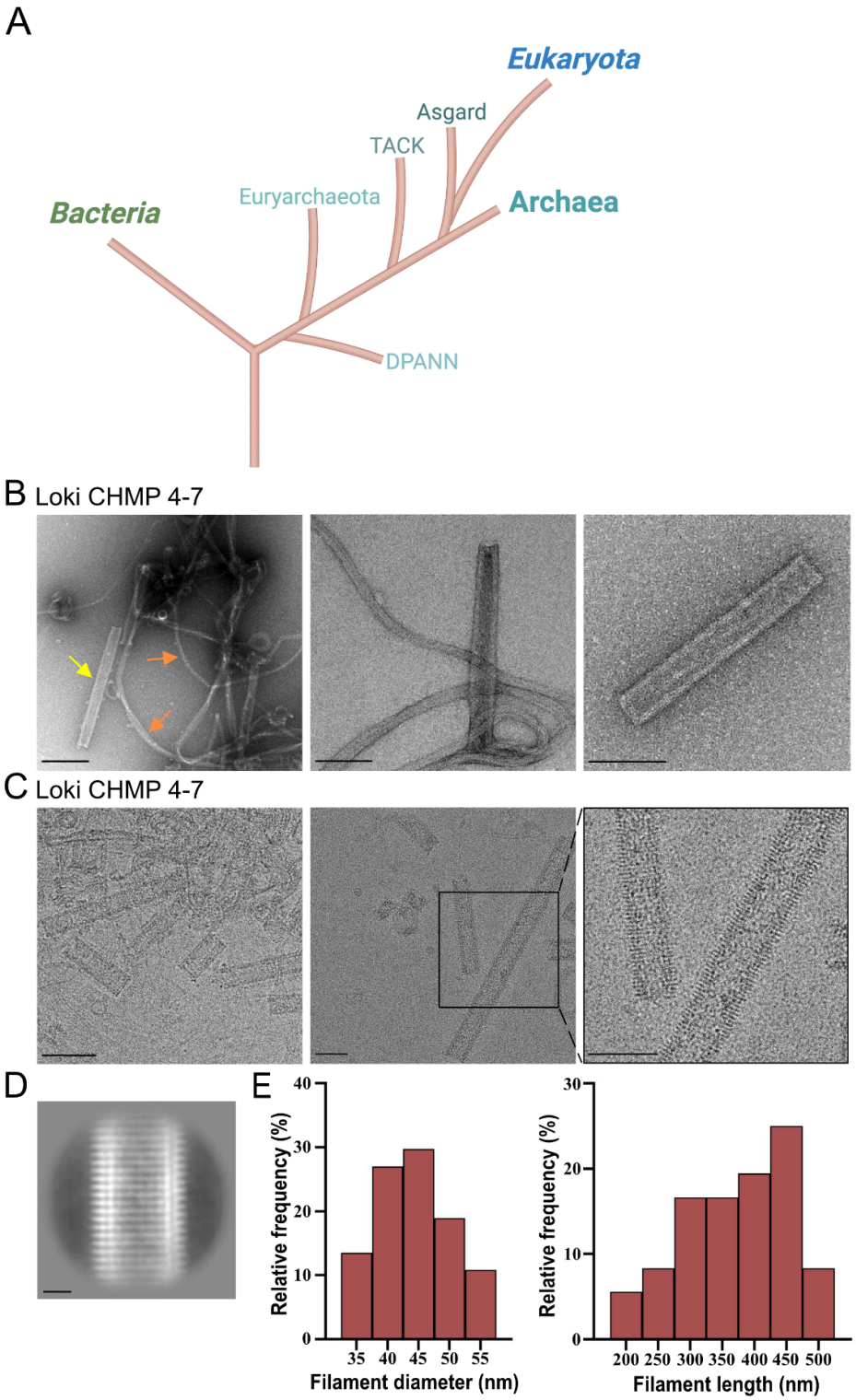

794

795 **Fig 1. Loki CHMP4-7 self-assembles into helical tubes.**
796 **A.** Schematic representation of the currently suggested models for the evolutionary
797 relationships between Bacteria, Archaea, and Eukarya that integrate the archaeal
798 Asgard clade. **B**. Negative-stain TEM micrographs of Loki CHMP4-7 homo-polymers.
799 Representative zoomed-out (left, scale = 200 nm) and zoomed-in (middle and right,
800 scale = 100 nm) images are shown. Orange arrows indicate proto-filaments, yellow
801 arrow indicates a helical tube. **C.** Representative Cryo-EM micrographs of Loki CHMP4-
802 7 homo-polymers. Left, scale = 100 nm, middle and right, scale = 50 nm. An
803 enlargement of the area depicted in black box in middle panel is show in right panel. **D.**
804 A representative 2D class average of 502 particles extracted from CHMP4-7
805 projections. Scale = 100 Å. **E.** Frequency histograms of Loki CHMP4-7 helical
806 diameters (left, n = 37) and length (right, n = 36) obtained from negative stain TEM
807 images acquired from two independent experiments. Averaged CHMP4-7 helical tube
808 diameter 44 ± 30.9 nm.
809
810

A CHMP 4-7

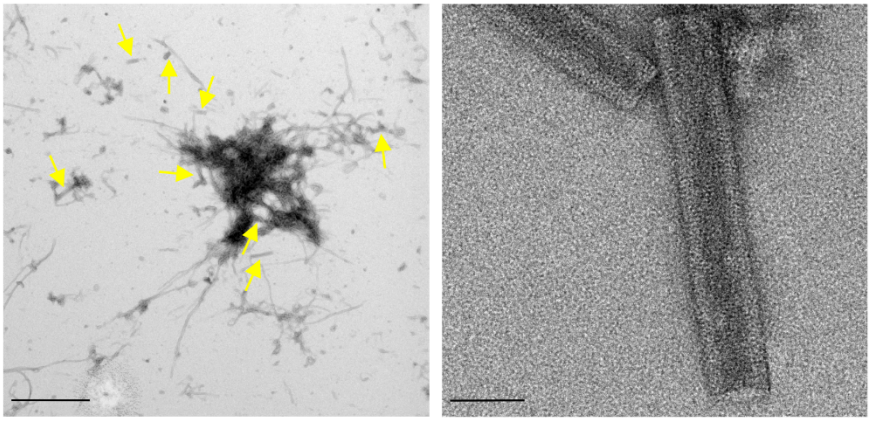

CHMP 4-7 - CHMP 1-3

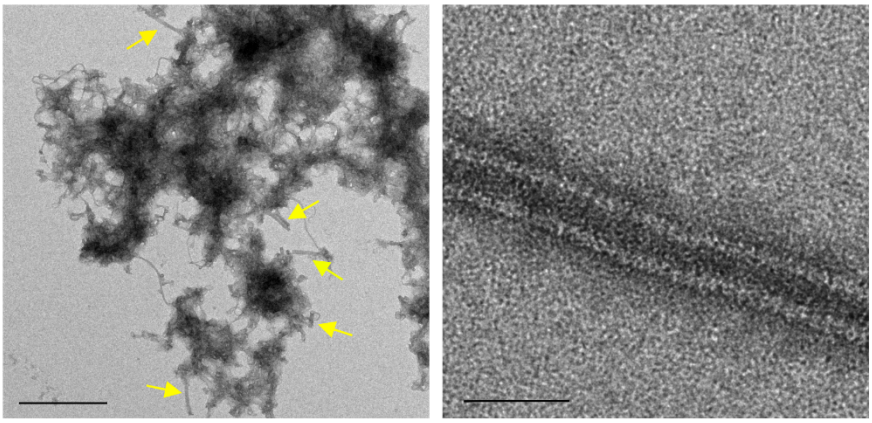

B

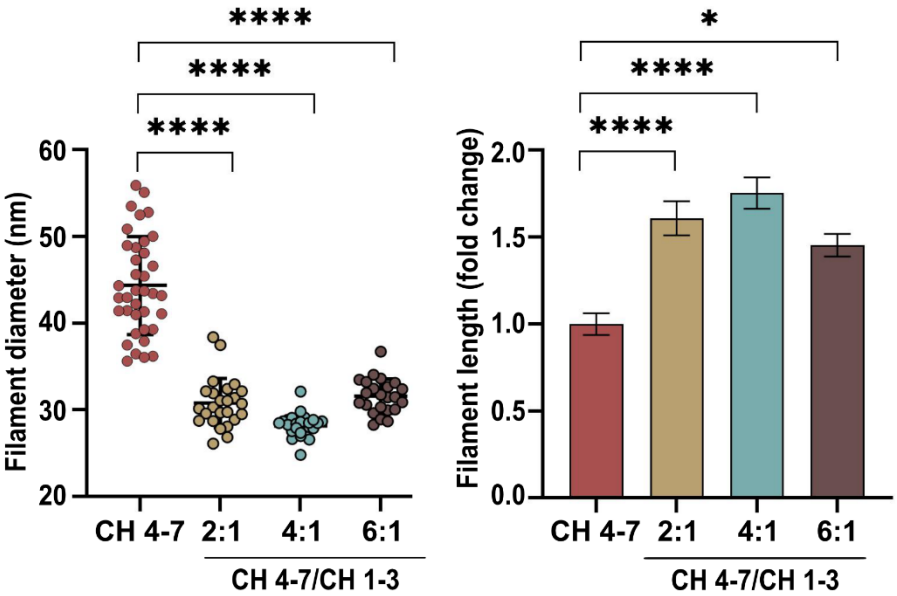

812 **Fig 2. CHMP1-3 induces morphological changes in Loki ESCRT-III helical tubes**
813 **A.** Representative negative-stain TEM images of Loki CHMP4-7 homo-polymers (upper
814 panels) and CHMP4-7-CHMP1-3 co-polymers (bottom panels, 4:1 molar ratio).
815 Zoomed-out (left, scale = 1 μm) and zoomed-in (right, scale = 50 nm) images are
816 shown. Yellow arrows indicate helical tubes. Note, that the helical tube in co-polymers is
817 more curved and displays periodic stripes that are not seen in the homo-polymers by
818 negative staining **B**. Diameter (left) and length (right) measurements of CHMP4-7-
819 CHMP1-3 helical-tubes that were assembled at the indicated molar ratios.
820 Measurements were obtained from negative stain TEM images. Averaged diameters
821 (nm): 2:1 ratio, 31 ± 7.7, n=25; 4:1 ratio 28 ± 1.6, n=26, 6:1 ratio 32 ± 3.8, n=23. One-
822 way analysis of variance (ANOVA) Kruskal-Wallis test followed by Dunn's post hoc test
823 was performed (see methods). Averaged lengths (nm): 2:1 ratio 641 ± 173, n=25; 4:1
824 ratio 594 ± 158, n=27; 6:1 ratio 492 ± 109, n=25

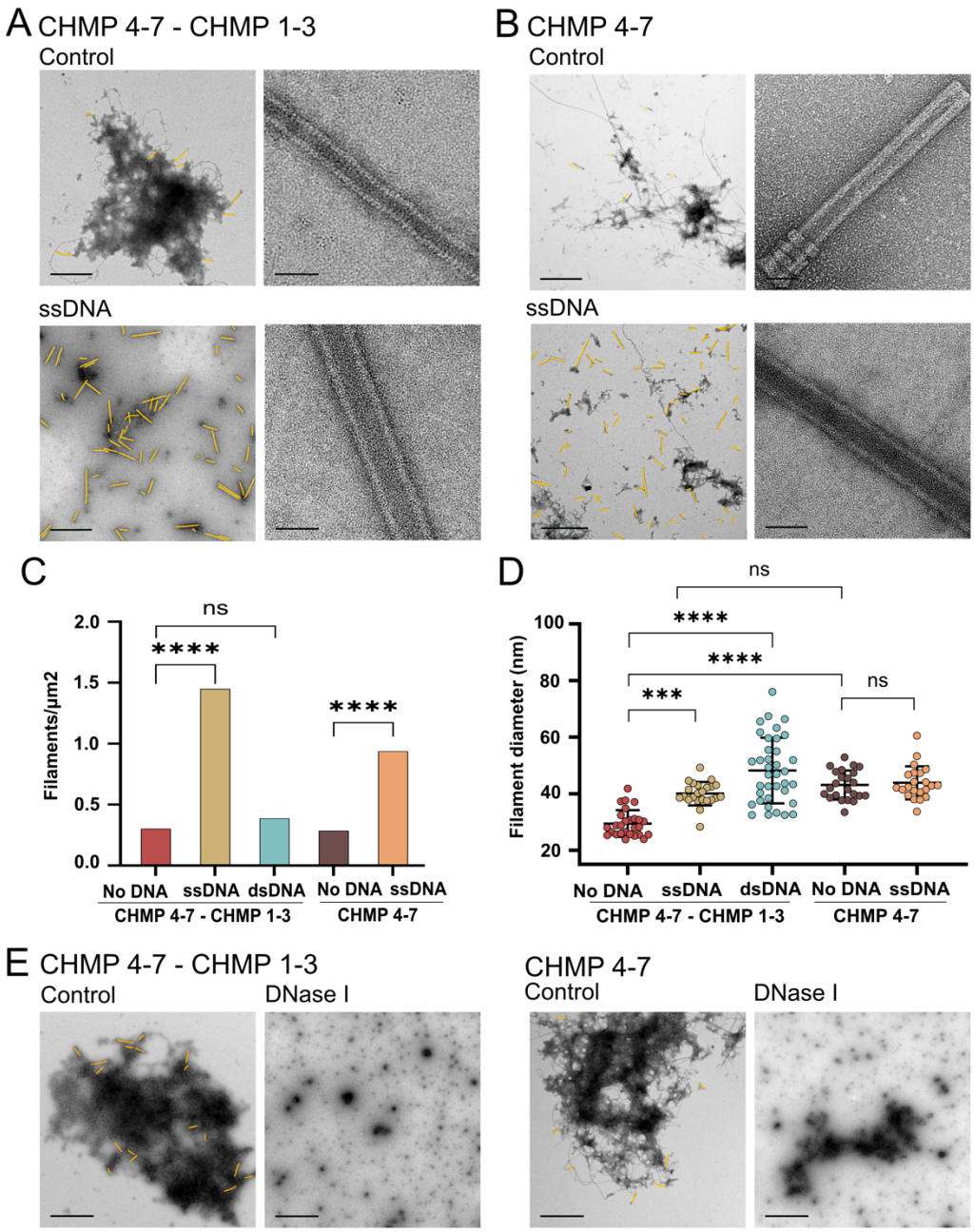
A CHMP 4-7 - CHMP 1-3
Control
ssDNA
B CHMP 4-7
Control
ssDNA
C
Filaments/µm2
2.0
1.5
1.0
0.5
0.0
ns
****
****
No DNA
ssDNA
dsDNA
No DNA
ssDNA
CHMP 4-7 - CHMP 1-3
CHMP 4-7
D
Filament diameter (nm)
100
80
60
40
20
ns
****
****
***
ns
No DNA
ssDNA
dsDNA
No DNA
ssDNA
CHMP 4-7 - CHMP 1-3
CHMP 4-7
E CHMP 4-7 - CHMP 1-3
Control
DNase I
CHMP 4-7
Control
DNase I

826 **Fig 3. DNA facilitates Loki ESCRT-III helical-tube assembly.**
827 **A-D** Loki ESCRT-III proteins CHMP4-7 and CHMP1-3 (4:1 molar ratio) (**A**) or CHMP4-7
828 alone (**B**) were subjected to plomerization reaction (see methods) in the absence or
829 presence of 40 bases oligonucleotides (ssDNA or dsDNA, as indicated), and
830 documented using negative-stain TEM. Representative zoomed-out (left, Scale = 1 μm)
831 and zoomed-in (right, Scale = 50 nm) images are shown in **A-B** and in Fig. S3A-B.
832 Helical tubes are colored in yellow in zoomed-out images (raw images, Fig. S3A). **C.**
833 Helical tubes density at various conditions. Measurements were performed on an area
834 >565 μm^2 from each experiment. Data from two independent experiments are
835 presented for each condition. **D.** Diameters of CHMP4-7 and CHMP4-7/CHMP1-3
836 helical tubes assembled in the presence of oligonucleotides. Averaged diameters (nm):
837 CHMP4-7/CHMP1-3 29.4 ±4.6, n=27; CHMP4-7/CHMP1-3 ssDNA 40±4.1, n=23;
838 CHMP4-7/CHMP1-3 dsDNA 48±11.5, n=37; CHMP4-7 43±5, n=23; CHMP4-7 ssDNA
839 44 ± 5.7, n = 22. **E**. Loki ESCRT-III proteins CHMP4-7 and CHMP1-3 (4:1 molar ratio)
840 (left) or CHMP4-7 alone (right) were assembled under control conditions, or in the
841 presence of 20 mg/ml DNase, as indicated. Helical tubes are colored in yellow (raw
842 images, Fig. S3E). Scale = 1 μm. Data was reproduced in four independent
843 experiments. Statistics in C and D was performed using one-way analysis of variance
844 (ANOVA) (see methods).
845
846
847
848
849
850
851
852
853
854
855
856

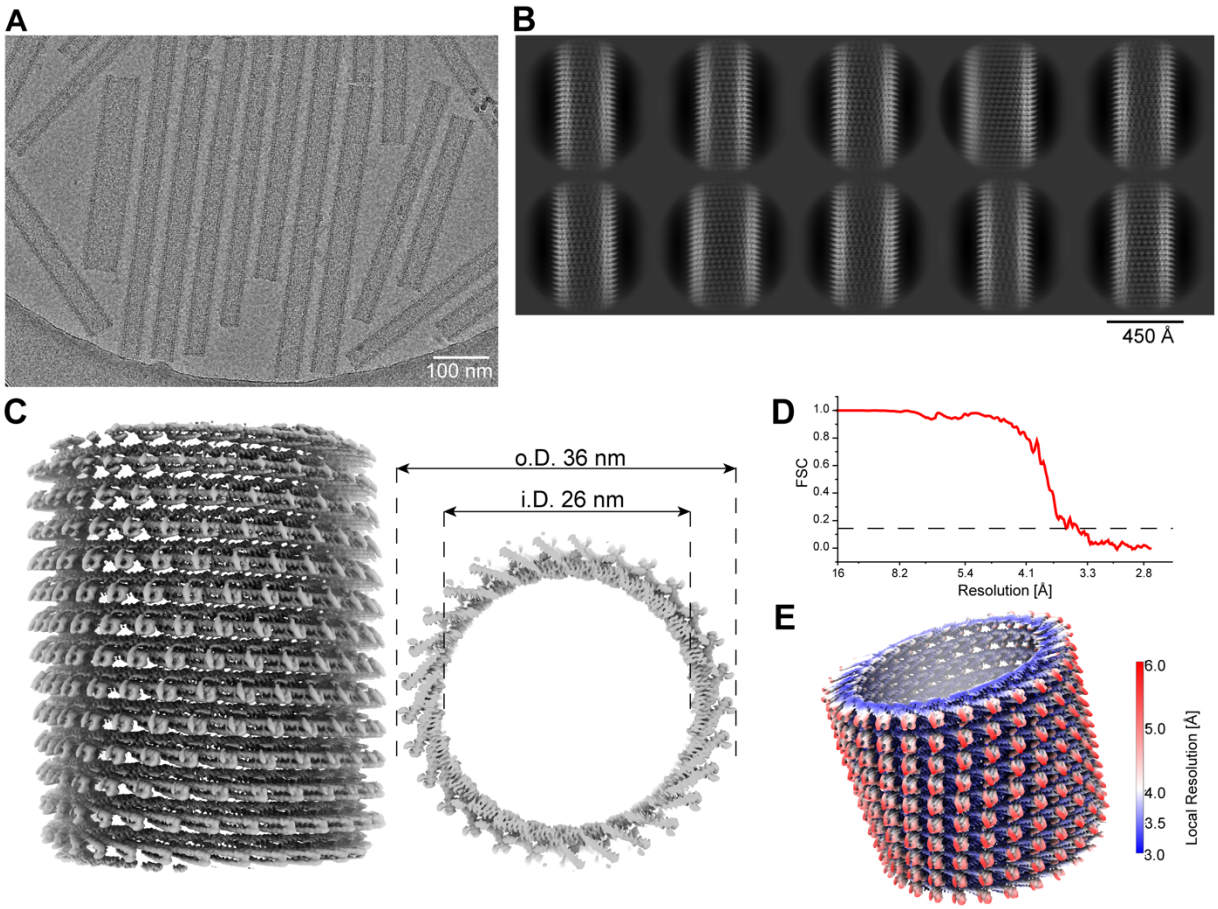

Fig 4. Loki CHMP4-7 forms PspA-like rod structures.

A. Example cryo-EM micrograph of Loki CHMP4-7 showing straight rod structures with different diameters. **B.** Set of 2D class averages of Loki CHMP4-7 rods with the typical Christmas tree pattern of PspA rods. **C.** Side (left) and top (right) view of cryo-EM density map of the rod structure with an inner and diameter of 26 and 36 nm, respectively. **D.** Fourier shell correlation of the cryo-EM density map indicating a nominal resolution at 3.6 Å according to the FSC 0.143 cutoff. **E.** Estimates of local resolution mapped in color code (blue=3.0 and red 6.0 Å resolution, respectively) on the cryo-EM density.

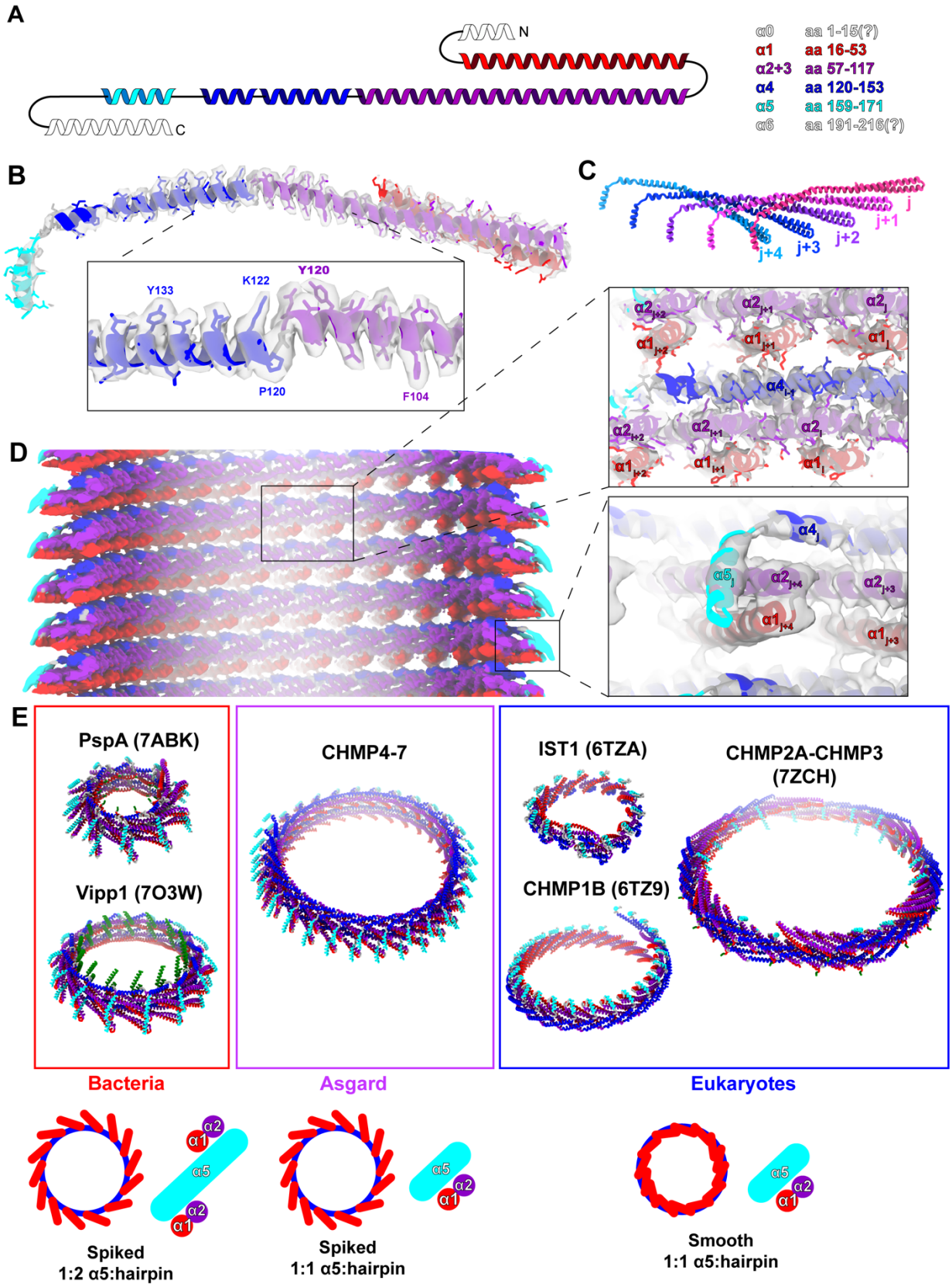
A
N
C
α0 aa 1-15(?)
α1 aa 16-53
α2+3 aa 57-117
α4 aa 120-153
α5 aa 159-171
α6 aa 191-216(?)
B
Y133
K122
Y120
P120
F104
C
j
j+1
j+2
j+3
j+4
D
E
PspA (7ABK)
Vipp1 (7O3W)
CHMP4-7
IST1 (6TZA)
CHMP1B (6TZ9)
CHMP2A-CHMP3
(7ZCH)
Bacteria
Asgard
Eukaryotes
α1
α2
α5
Spiked
1:2 α5:hairpin
Spiked
1:1 α5:hairpin
Smooth
1:1 α5:hairpin

869

870 **Fig 5. Loki CHMP4-7 rods are built from monomers sharing typical ESCRT-III**
871 **features.**
872 **A.** Topology plot of the Loki CHMP4-7 structure with color-coded helices: α0 white, α1
873 red, α2+3 violet, α4 blue, α5 cyan, α6 white. **B.** Segmented density including modeled
874 atomic Loki CHMP4-7 monomer structure (inset visible side-chains aa 104-134) found
875 in 36 nm rods showing the ESCRT-III fold. **C.** Organization of the CHMP 4-7 monomers
876 in the helical assembly: α5 of chain j interacts with the hairpin of chain j+4. **D.** Cryo-EM
877 map of Loki CHMP4-7 rod with isosurface colored CHMP 4-7 α-helices and enlarged
878 view of the cryo-EM map with the fitted model showing the interactions in the tube wall
879 and helix α5 interactions in the periphery. **E.** Comparison of tubular ESCRT-III
880 assemblies from bacteria, Asgard archaea and eukaryotes. PspA: 7abk, Vipp1: 7o3w,
881 IST1: 6tza, CHMP1B: 6tz9, CHMP2A-CHMP3: 7zch. Color-coded helices: α0 green, α1
882 red, α2+3 violet, α4 blue, α5 cyan.

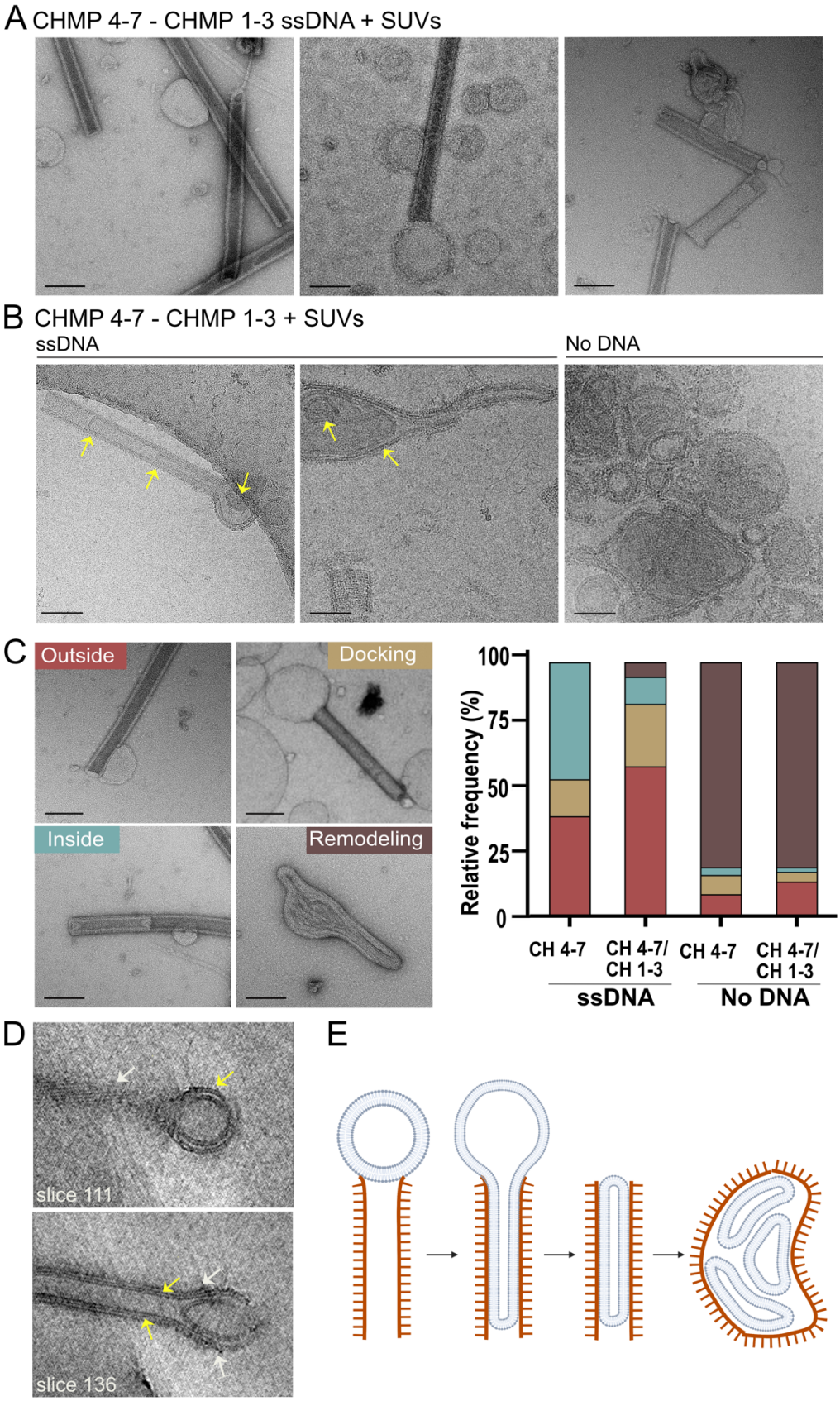
A CHMP 4-7 - CHMP 1-3 ssDNA + SUVs
B CHMP 4-7 - CHMP 1-3 + SUVs
ssDNA
No DNA
C
Outside
Docking
Inside
Remodeling
Relative frequency (%)
100
75
50
25
0
CH 4-7
CH 4-7/ CH 1-3
CH 4-7
CH 4-7/ CH 1-3
ssDNA
No DNA
D
slice 111
slice 136
E

884 **Fig 6. Loki ESCRT-III filaments deform eukaryotic-like membrane vesicles**
885 **A-B.** Representative negative-stain TEM (**A**) and cryo-EM (**B**) images of CHMP4-7-
886 CHMP1-3 helical tubes (molar ratio, 4:1) assembled in the presence of ssDNA (10 μM),
887 and incubated with SUVs (DOPC:DOPS, 1:1 ratio). Scale = 100 nm. Arrows in **B** specify
888 internalized vesicles. **C**. Percentages of the different types of vesicle-tube interactions
889 observed under the specified conditions. Left panel, representative negative-stain
890 images of the four types of interactions quantified. Outside (type 1); Docking (type 2);
891 Inside (type 3); Remodeling (type 4). Data was quantified from negative stain images
892 obtained from at least two independent experiments for each condition (n = CHMP4-7
893 ssDNA, 124; CHMP4-7-CHMP1-3 ssDNA, 159; CHMP4-7, 197; CHMP4-7-CHMP1-3,
894 161). Scale = 100 nm. Pearson chi-squared analysis show a significant difference in the
895 distributions of homo- and co-polymers assembled in the presence vs absence of DNA
896 (p- value ≤ 0.0001 for all pairs). No significance was found in the distributions obtained
897 for ESCRT-III filaments assembled in the presence or absence of CHMP 1-3 that were
898 subjected to similar treatments. Scale =1 μm. **D**. Selected slices of reconstructed
899 tomograms of filaments-SUV complexes showing the membrane (yellow arrows) and
900 ESCRT-III filament (white arrows). The complete series is provided in Sup. movies 1. **E.**
901 A suggested model for Loki ESCRT-III mediated vesicle remodeling. Vesicles docked at
902 the tip of the ESCRT-III tube directly interact with the interior of the tube, leading to
903 deformation and invagination of the vesicle by the ESCRT-III filament. This process
904 occurs repeatedly, leading to the formation of a complex membrane network inside the
905 helical tube, which ultimately causes deformation and remodeling of the ESCRT-III tube.
906 Tube remodeling is inhibited in the presence of DNA, resulting in the accumulation of
907 ESCRT-III-SUV interactions in all the stages that precede this stage.
908
909
910
911
912
913
914

915 SUPPLEMENTARY FIGURES

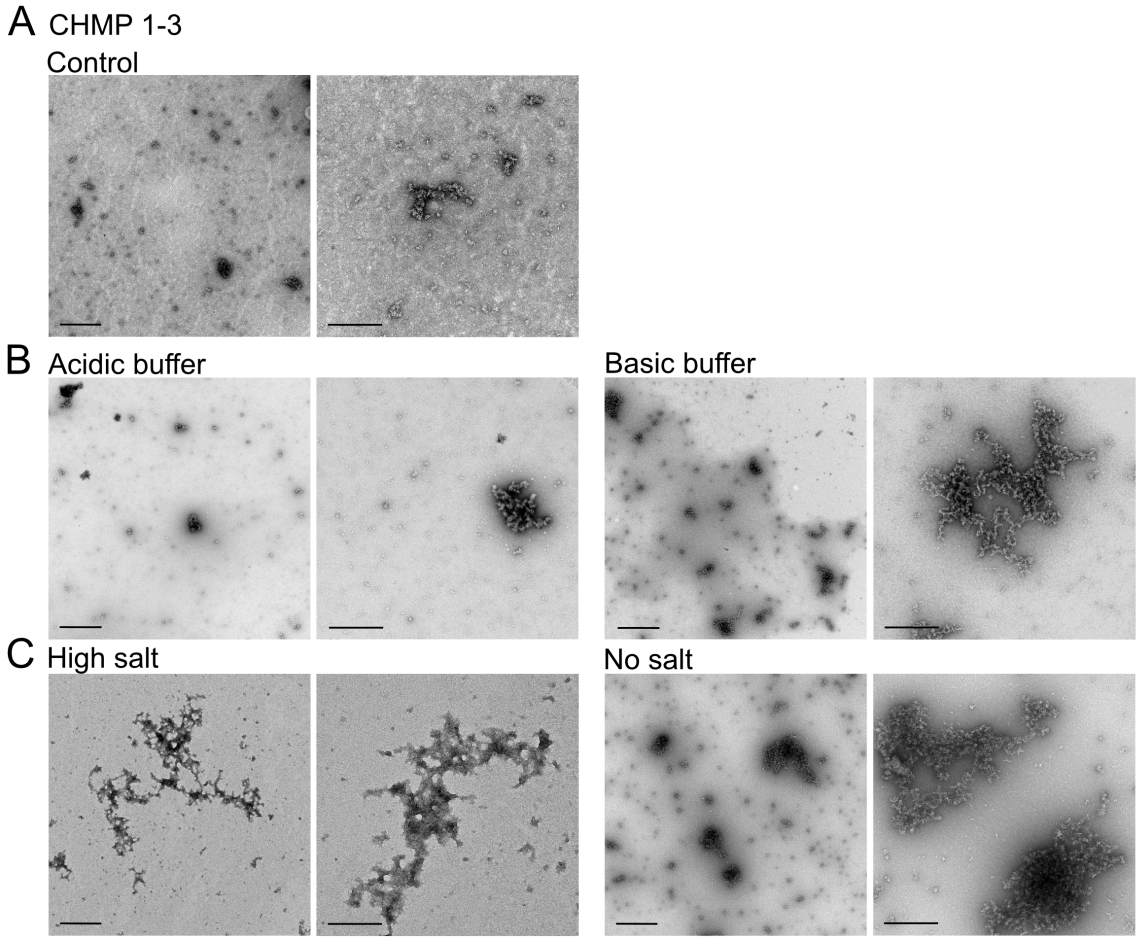

916

917 **Fig S1: Loki CHMP1-3 do not self-assemble into high-ordered structures.** (**A-C**)
918 representative negative stain TEM images of full-length Loki CHMP1-3 that was
919 subjected to polymerization reaction at different buffers. (**A**) buffer used for CHMP4-7
920 self-assembly: 25 mM Tris pH=7.6, 50 mM KCl). (**B**) Using acidic (50 mM Sodium
921 Acetate pH=5, 50 mM KCl) or basic (25 mM Tris pH=8.8 50 mM KCl buffers). (**C**) at
922 different ionic strengths (high salt: 25 mM Tris pH=7.6, 200 mM KCl; No salt: 25 mM
923 Tris pH=7.6. A final concentration of 10.88 μM CHMP1-3 was used for all buffer
924 conditions. No filaments were observed under any of the examined conditions.

A CHMP 4-7 - CHMP 1-3 (2:1)

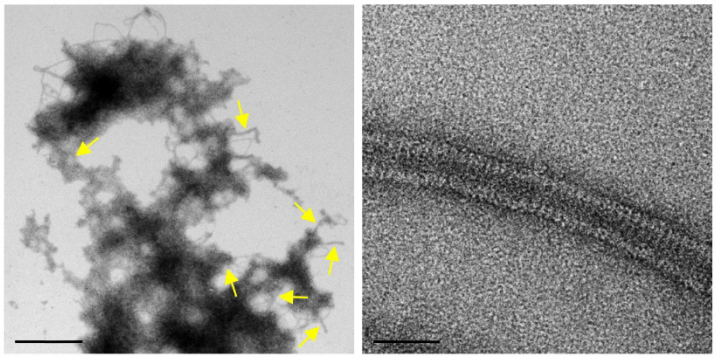

CHMP 4-7 - CHMP 1-3 (6:1)

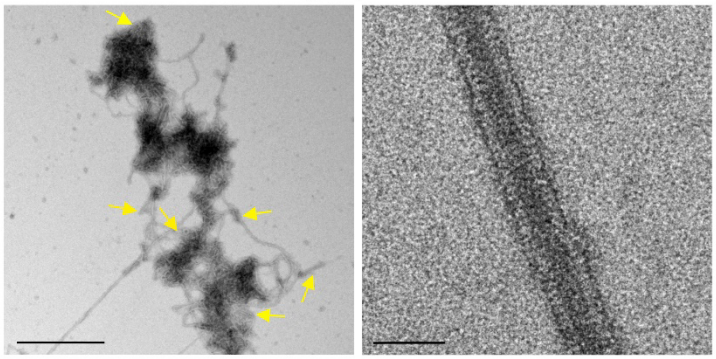

B CHMP 4-7 - CHMP 1-3 ssDNA

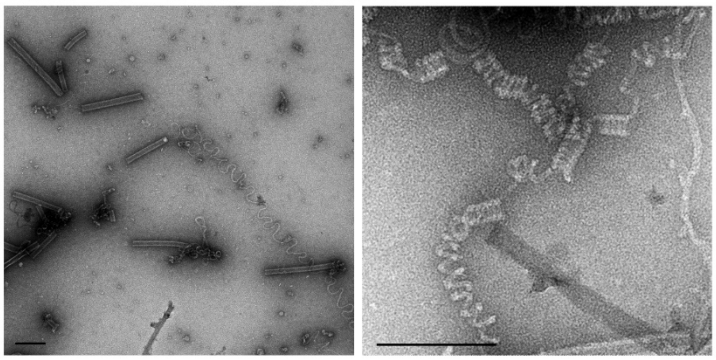

C CHMP 4 -7

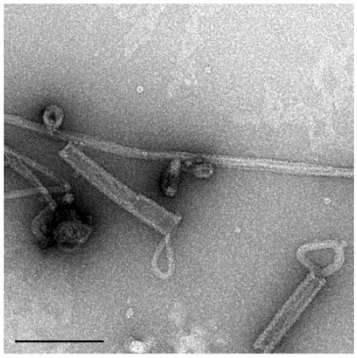

CHMP 4-7 - GFP

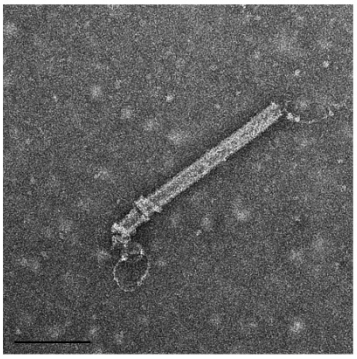

926 **Fig. S2: Characterization of Loki ESCRT-III filaments. A.** Representative negative
927 stain TEM images of Loki ESCRT-III filaments assembled using CHMP4-7 and CHMP1-
928 3 at molar ratios 2:1 (upper panel) and 6:1 (bottom panel). Zoomed-out (left, Scale = 1
929 μm); zoomed-in (right, Scale = 50 nm). Yellow arrows indicate helical tubes.
930 Corresponds to measurements in Fig. 2B. **B.** Negative stain TEM images of loose Loki
931 Loki ESCRT-III filaments assembled in the presence of CHMP4-7 – CHMP1-3 (2:1
932 molar ratio, ssDNA) resembling a telephone cord, supporting that the ESCRT-III tube is
933 composed of a packed helical filament. Scale = 200 nm **C.** Representative negative
934 stain TEM images of filaments assembled in the presence of Loki CHMP 4-7 at a total
935 concentration that equals the concentration of both CHMP4-7 - CHMP1-3 at 2:1 ratio
936 (left, final concentration of 16 μM) and in the presence of both CHMP4-7 and purified
937 recombinant GFP (right panel), reaching the same final concentrations (CHMP 4-7
938 10.67 μM, GFP 5.4 μM). Scale = 200 nm. No effect on filament formation was identified
939 under these assembly conditions. Data in all panels was reproduced in at least two
940 independent experiments.
941

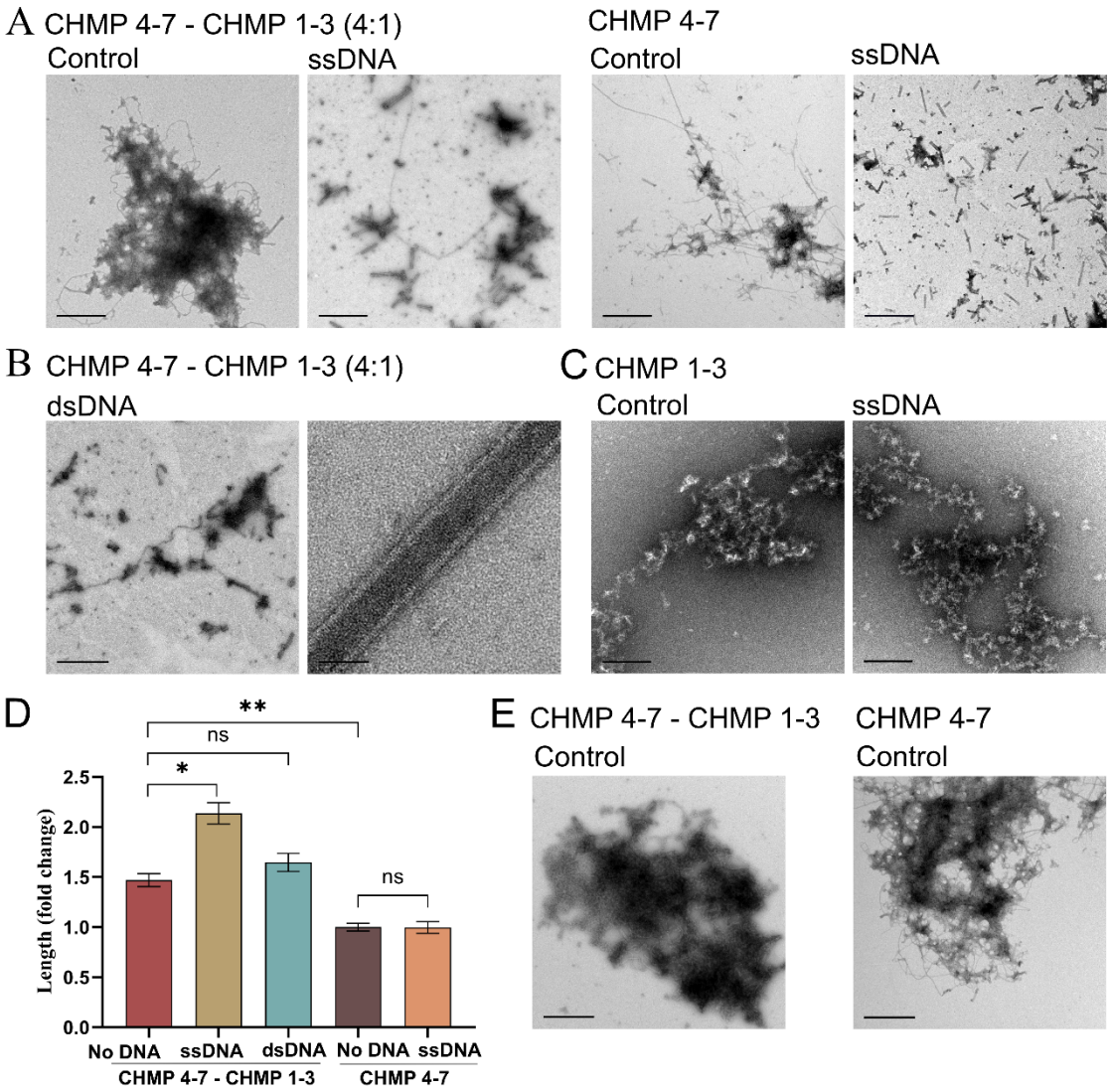
A CHMP 4-7 - CHMP 1-3 (4:1)
Control
ssDNA
CHMP 4-7
Control
ssDNA
B CHMP 4-7 - CHMP 1-3 (4:1)
dsDNA
C CHMP 1-3
Control
ssDNA
D
**
ns
*
ns
Length (fold change)
2.5
2.0
1.5
1.0
0.5
0.0
No DNA
ssDNA
dsDNA
No DNA
ssDNA
CHMP 4-7 - CHMP 1-3
CHMP 4-7
E CHMP 4-7 - CHMP 1-3
Control
CHMP 4-7
Control

943 **Fig. S3: Helical tube formation by Loki ESCRT-III in the presence of nucleic acids.**
944 **A.** Raw data of the representative zoomed-out negative stain TEM images presented in
945 Fig. 3A. Scale = 1 μm. **B.** CHMP4-7 and CHMP1-3 (4:1 molar ratio) were subjected to
946 polymerization reaction (see methods) in the presence of 40 bases dsDNA, and
947 documented using negative-stain TEM. Scale zoomed out, 1 μm; zoomed in, 50 nm **C.**
948 Representative zoomed-out negative stain TEM images of assembly reactions using
949 Loki CHMP 1–3 with or without ssDNA (40 bases probe) showing that addition of
950 ssDNA does not induce polymerization of CHMP 1-3. Scale = 200 nm. **D.** Length
951 measurements of helical tubes formed under the indicated conditions (corresponds to
952 Fig. 3). Measurements obtained from negative stain TEM images of samples produced
953 in at least two independent experiments for each condition. Averaged lengths (nm):
954 CHMP4-7/CHMP1-3 534.8 ±118.8, n=25; CHMP4-7/CHMP1-3 ssDNA 777.5 ±210.6,
955 n=30; CHMP4-7/CHMP1-3 dsDNA 599±218.2, n=45; CHMP4-7 364±67.8, n=23;
956 CHMP4-7 ssDNA 363 ± 96.1, n = 21. **E.** Raw data of the representative zoomed-out
957 negative stain TEM images presented in Fig. 3E.
958
959

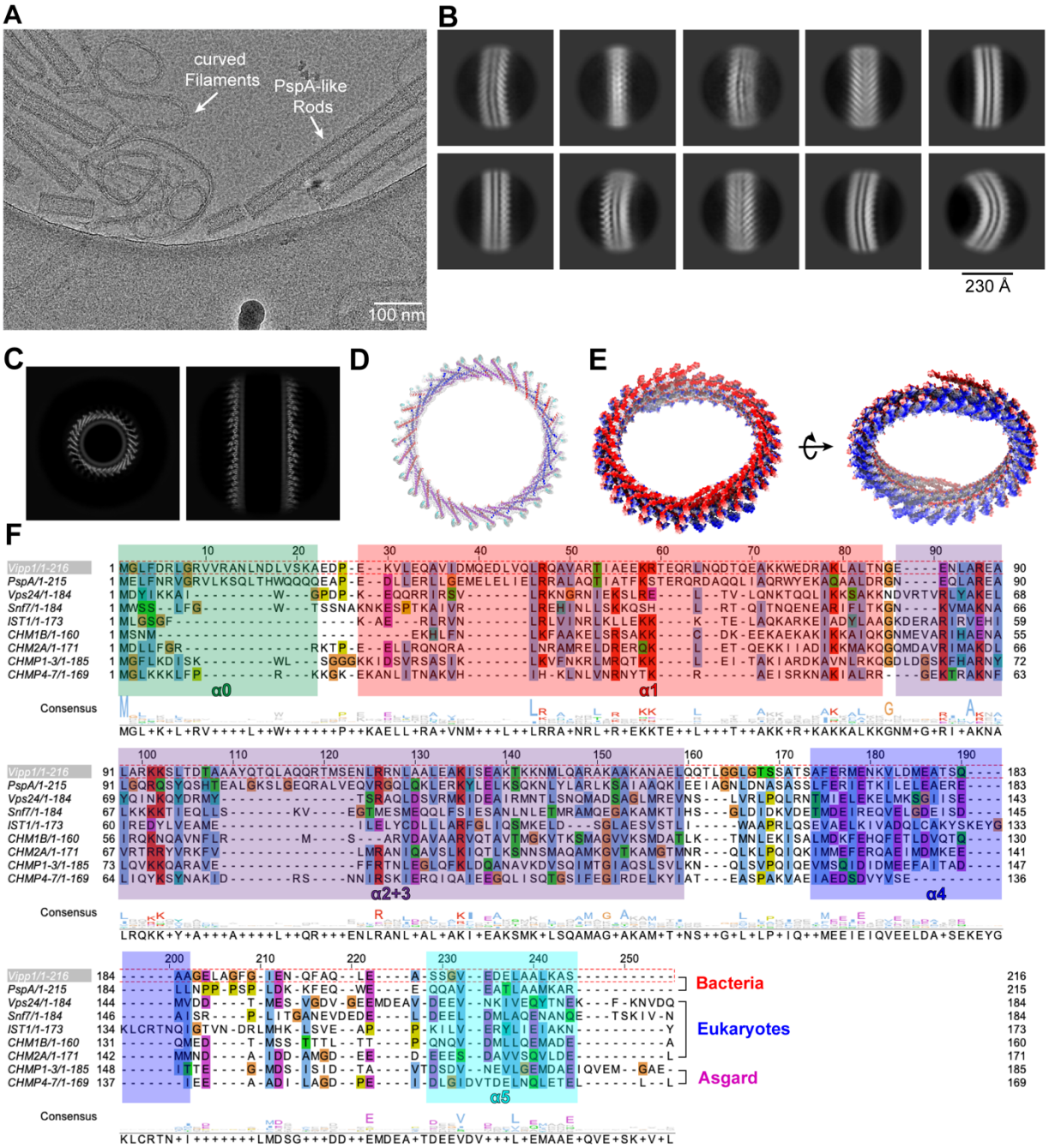

Fig. S4: Curved Filaments and ESCRT-III comparison.

A. Cryo-EM micrograph of CHMP 4-7/CHMP 1-3 (4:1 molar ratio, assembled in the presence of ssDNA) showing curved filaments and PspA-like rods. **B.** 2D class averages of curved filaments. **C.** z and xy slice (averaged over 10 px) of the Loki CHMP4-7 rods showing tube-like fuzzy density in the lumen of the rods. **D.** Top view of the density map and the fitted polymer model. **E.** Electrostatic surface of helical

967 assembly reveals a negatively and a positively charged end indicating a distinct polarity
968 of the rod. **F.** Sequence alignment of ESCRT-III proteins with known structures
969 (truncated to α5) in comparison with Loki CHMP 1-3 and 4-7. The alignment is
970 superimposed with the consensus secondary structures derived from the deposited
971 models. Residues with similarity >30% are colored according to their properties
972 (ClustalX color scheme). Sequences were aligned using the T-Coffee webserver and
973 visualized with JalView (*50, 51*).

A CHMP 4-7 - CHMP 1-3 + DOPC : DOPS

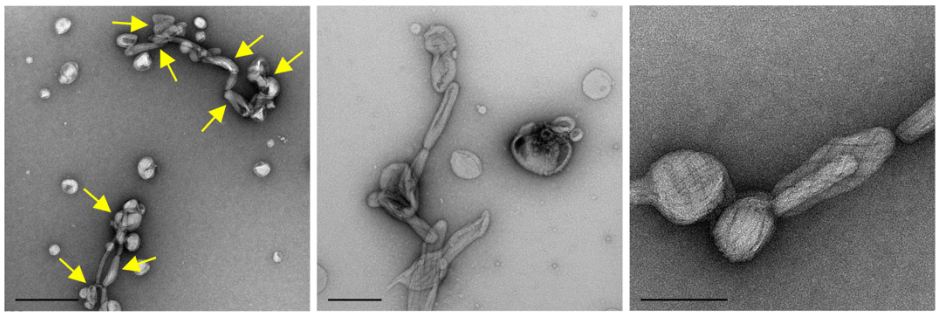

CHMP 4-7 ssDNA + DOPC : DOPS

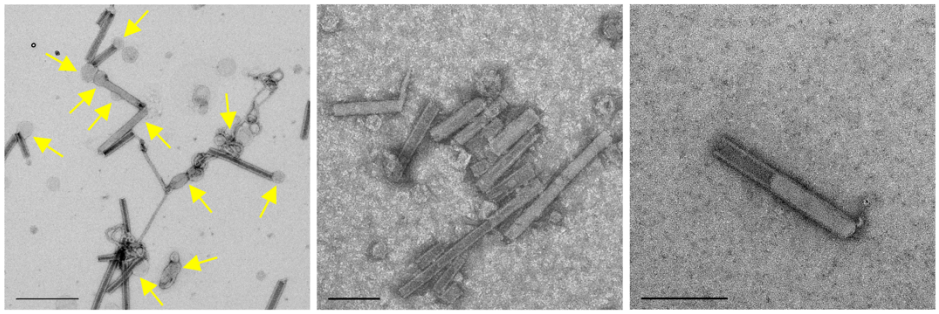

CHMP 4-7 + DOPC : DOPS

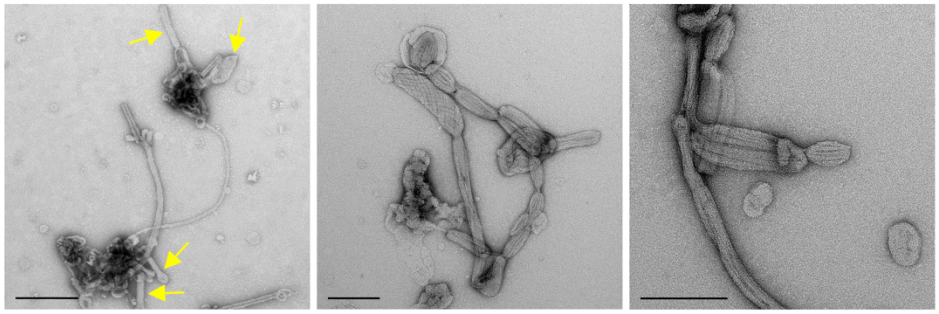

B DOPC : DOPS

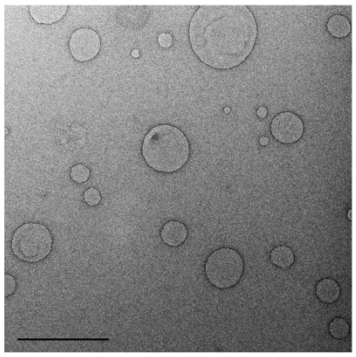

C

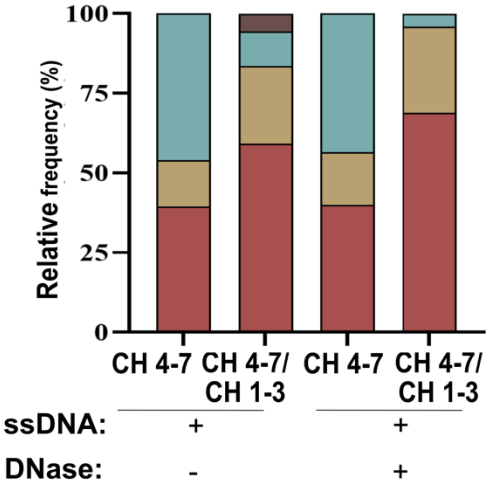

975 **Fig. S5: Interactions of Loki ESCRT-III filaments with negatively charged SUVs**
976 **(DOPC**:**DOPS 1:1). A.** Representative negative stain TEM images of Loki ESCRT-III
977 filaments that were assembled at the indicated conditions and incubated for 1hour with
978 DOPC:DOPS SUVs. Zoom out images are shown on left panels. Arrows indicate
979 interactions between SUVs and filaments. Corresponds to quantification shown in Fig.
980 6C. Scale left panels = 500 nm, middle and right panels =200 nm. **B.** A representative
981 negative stain TEM image of DOPC:DOPS SUVs prior to incubation with Loki ESCRT-
982 III. (Scale = 500 nm). **C.** Effect of DNase on pre-assembled ESCRT-III-SUV complexes.
983 ESCRT-III-SUV complexes were generated as in A and were subjected (or not) to
984 DNase treatment and the distribution of the different vesicle-tube interactions observed
985 under the specified conditions was quantified. Note that DNase was not able to disrupt
986 pre-assembled ESCRT-III-SUV interactions (categories are as in Fig. 6C).

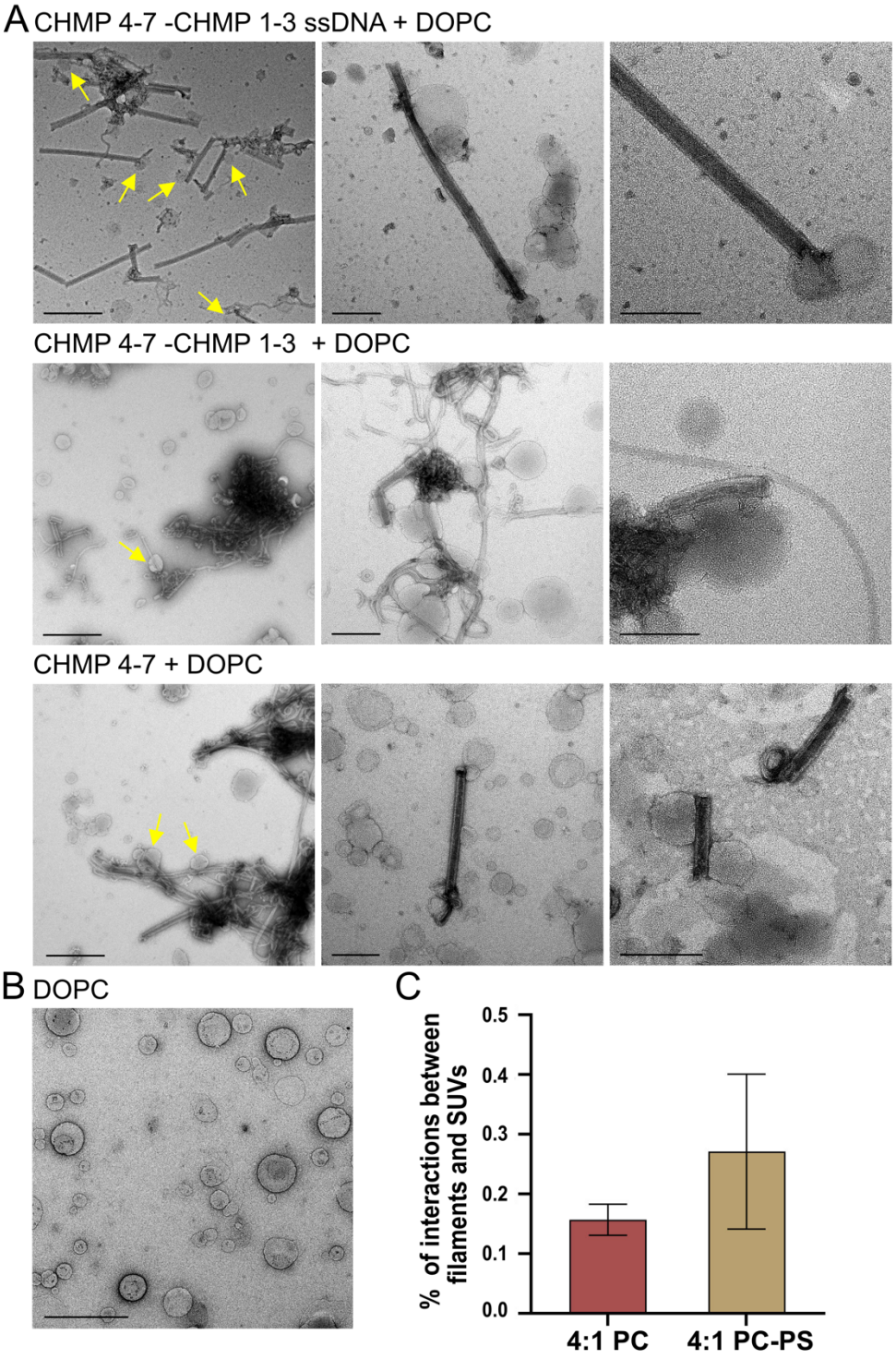
A CHMP 4-7 -CHMP 1-3 ssDNA + DOPC
CHMP 4-7 -CHMP 1-3 + DOPC
CHMP 4-7 + DOPC
B DOPC
C
% of interactions between filaments and SUVs
0.5
0.4
0.3
0.2
0.1
0.0
4:1 PC
4:1 PC-PS

988 **Fig. S6: Interactions of Loki ESCRT-III filaments with DOPC SUVs. A.**
989 Representative negative stain TEM images of Loki ESCRT-III filaments that were
990 assembled at the indicated conditions and incubated for 1hour with DOPC SUVs. Zoom
991 out images are shown on left panels. Arrows indicate interactions between SUVs and
992 filaments. Scale: left panels = 500 nm, middle and right panels =200 nm. Note that the
993 most prominent interaction is adhesion of the vesicle to the outside of the tube. **B.**
994 representative negative stain TEM image of DOPC SUVs prior to incubation with Loki
995 ESCRT-III. (Scale = 500 nm). **C.** Percentages of interactions between Loki CHMP 4-7 –
996 CHMP 1-3 (4:1) filaments with SUVs comprised of DOPC or DOPC-DOPS (1:1),
997 showing preference to DOPS containing vesicles.
998